

# 1 Quantifying the Influence of Mutation Detection on 2 Tumour Subclonal Reconstruction

3 **Lydia Y. Liu**<sup>1,2,3,4,5,6,†</sup>, **Vinayak Bhandari**<sup>1,†</sup>, **Adriana Salcedo**<sup>1,4,5,6,7</sup>, **Shadrielle M. G. Espiritu**<sup>7</sup>,  
4 **Quaid D. Morris**<sup>3,8,9,10</sup>, **Thomas Kislinger**<sup>1,2</sup>, **Paul C. Boutros**<sup>1,3,4,5,6,11,12,\*</sup>

5  
6 <sup>1</sup> Department of Medical Biophysics, University of Toronto, Toronto, ON M5G 1L7, Canada

7 <sup>2</sup> Princess Margaret Cancer Centre, University Health Network, Toronto, ON M5G 2C1, Canada

8 <sup>3</sup> Vector Institute for Artificial Intelligence, Toronto, ON M5G 1M1, Canada

9 <sup>4</sup> Department of Human Genetics, University of California, Los Angeles, 90095

10 <sup>5</sup> Jonsson Comprehensive Cancer Centre, University of California, Los Angeles, 90095

11 <sup>6</sup> Institute for Precision Health, University of California, Los Angeles, 90095

12 <sup>7</sup> Ontario Institute for Cancer Research, Toronto, ON M5G 0A3, Canada

13 <sup>8</sup> Department of Computer Science, University of Toronto, Toronto, ON M5T 3A1, Canada

14 <sup>9</sup> Department of Molecular Genetics, University of Toronto, Toronto, ON M5S 1A8, Canada

15 <sup>10</sup> Donnelly Centre for Cellular and Biomolecular Research, University of Toronto, Toronto, ON M5S 3E1, Canada

16 <sup>11</sup> Department of Pharmacology and Toxicology, University of Toronto, Toronto, ON M5S 1A8, Canada

17 <sup>12</sup> Department of Urology, University of California, Los Angeles, 90095

18 \* Corresponding author

19 † These authors contributed equally to this work

20  
21 **Address for correspondence:**

22 Dr. Paul C. Boutros

23 12-109 CHS

24 10833 Le Conte Avenue

25 Los Angeles, California

26 90095

27 Email: [pboutros@mednet.ucla.edu](mailto:pboutros@mednet.ucla.edu)

28 Phone: 310-794-7160

## 29 **Abstract**

30 Whole-genome sequencing **can be used** to estimate subclonal populations in tumours and this **intra-**  
31 **tumoural** heterogeneity **is linked** to clinical outcomes. Many algorithms have been developed **for**  
32 subclonal reconstruction, but their variability and consistency **are** largely unknown. We evaluated  
33 **sixteen** pipelines for reconstructing the evolutionary histories of 293 localized prostate cancers  
34 from single samples, and **eighteen pipelines for the reconstruction of 10 tumours with** multi-region  
35 sampling. **Predictions of subclonal architecture and timing of somatic mutations vary extensively**  
36 across pipelines. **Pipelines show** consistent types of bias, with those **incorporating** SomaticSniper  
37 and Battenberg preferentially predicting homogenous cancer cell populations **and** those using  
38 MuTect tending to predict multiple populations of cancer cells. Subclonal reconstructions using  
39 multi-region sampling **confirm** that single-sample reconstructions systematically **underestimate**  
40 intra-tumoural heterogeneity, **predicting** on average fewer than half of the cancer cell populations  
41 identified by multi-region sequencing. **Overall**, these biases suggest caution in interpreting specific  
42 architectures and subclonal variants.

43

## 44 Introduction

45 Understanding tumour heterogeneity and subclonal architecture is important for the elucidation of  
46 the mutational and evolutionary processes underlying tumorigenesis and treatment resistance<sup>1-4</sup>.  
47 Many studies of tumour heterogeneity have focused on small patient cohorts with multi-region  
48 sequencing<sup>5-11</sup>. This study design allows the reconstruction of sample trees that illustrate the  
49 relationships between multiple primary and metastatic lesions using shared and private  
50 mutations<sup>6,11</sup>. Despite their small sample sizes, these studies have provided remarkable insight,  
51 demonstrating multiple subclones within a single tumour, clonal relationships between primary  
52 and metastatic tumours and evidence for multiple primary tumours within a single patient. Many  
53 studies have further delved into intra-tumoural heterogeneity and constructed clone trees that  
54 demonstrate the phylogenetic relationship between cancer cell populations that are shared or  
55 unique between lesions<sup>5,7,9,12</sup>. The latter analyses not only provide insight to the convergent and  
56 branching evolution of cancer, but also characterize cancer cell migration and highlight the  
57 subclonal complexity within individual lesions.

58 Some studies have applied these techniques to large cohorts of single region tumour whole  
59 genomes. For example, we reconstructed the subclonal architectures of 293 localized prostate  
60 cancers using whole-genome sequencing (WGS) of a single region of the index lesion<sup>13</sup>. The larger  
61 sample sizes of single-region studies allow the identification of mutational events that are biased  
62 to occur at specific times during tumour development. Single-region subclonal reconstruction  
63 studies have also suggested that patients with less subclonal diversity (e.g. with only a single  
64 detectable population of cancer cells; termed *monoclonal*) tend to have superior clinical outcomes  
65 compared to those with more subclonal diversity (e.g. those with highly *polyclonal* tumours)<sup>13</sup>.

66 A variety of algorithms have been developed to reconstruct the subclonal architecture of cancers  
67 from single-region or multi-region bulk DNA sequencing data<sup>14-21</sup>. These algorithms broadly  
68 attempt to infer cancer cell populations based on cancer cell fractions (the fraction of cancer cells  
69 in which each variant is present) of somatic single nucleotide variants (SNVs) and/or somatic copy  
70 number aberrations (CNAs). Several employ Bayesian models to cluster mutations, and estimate  
71 the number and prevalence of cancer cell populations<sup>15-17,20,22</sup>. Some algorithms are further able  
72 to infer phylogenetic clone trees, thus resolving the evolutionary relationship between mutation  
73 clusters<sup>15,21</sup>. However, there has not been a systematic comparison of the features and consistencies

74 of their reconstructions on a large dataset. It is thus unclear to what extent these pipelines agree on  
75 large cohorts of real data, whether specific pipelines are biased towards certain types of  
76 reconstructions, and to what degree reconstruction results are influenced by the somatic mutation  
77 inputs. It is further unclear to what extent single-sample reconstructions differ from multi-region  
78 reconstructions, raising questions on the magnitude of underestimation present in large-cohort  
79 studies.

80 To address these gaps in the field, we evaluated pipelines consisting of twenty-two different  
81 combinations of well-established and independent SNV detection tools, subclonal CNA detection  
82 tools and subclonal reconstruction algorithms. Sixteen pipelines were applied to a set of 293 high-  
83 depth tumour-normal pairs<sup>13,23</sup> and eighteen were applied to 10 tumours with multi-region  
84 sequencing<sup>8,24</sup>. We quantify differences in the predictions of subclonal architecture, variant  
85 detection and downstream analyses, generating useful guidance for the community and a resource  
86 for improving existing methods and benchmarking new ones.

## 87 Results

### 88 Overview and Summary of Pipeline Runs

89 We reconstructed the subclonal architectures of 293 primary localized prostate tumours using  
90 sixteen pipelines (**Figure 1, Supplementary Table 1**). Each patient had WGS of a single region  
91 taken from the index lesion (**Methods**) that was macro-dissected to > 70% tumour cellularity  
92 (mean coverage  $\pm$  standard deviation [SD]:  $63.9 \pm 16.7$ ) and of matched blood reference tissue  
93 (mean coverage  $\pm$  SD:  $41.2 \pm 9.0$ ), as reported previously<sup>13</sup>. To investigate the influence of variant  
94 detection on subclonal reconstruction, we detected CNAs using Battenberg and TITAN<sup>7,25</sup> and  
95 SNVs using SomaticSniper and MuTect<sup>26,27</sup>. We then used the CNAs and SNVs detected by these  
96 tools in factorial combinations as inputs for four widely-used subclonal reconstruction algorithms:  
97 PhyloWGS<sup>15</sup>, DPCLust<sup>16</sup>, PyClone<sup>17</sup> and SciClone<sup>20</sup>. Each subclonal reconstruction pipeline was  
98 thus composed of three algorithms: a SNV detection tool, a subclonal CNA detection tool and a  
99 subclonal reconstruction algorithm. Thus “PhyloWGS-comprising pipelines” refers to all pipelines  
100 that use PhyloWGS as the subclonal reconstruction algorithm, in combination with any SNV and  
101 CNA detection tool. All subclonal reconstruction solutions were subjected to the same post-  
102 processing heuristics to minimize bias (**Methods**). We further quantified the variability that arises  
103 in subclonal reconstruction from spatially sampling the same tumour, focusing on ten tumours  
104 with multi-region WGS (2-4 regions per tumour, total of 30 regions)<sup>8,24</sup>. Multi-region WGS  
105 samples were further assessed using FACETS<sup>28</sup> for subclonal CNA detection, and subclonal  
106 reconstruction was performed both with all regions together and with each region individually  
107 using PhyloWGS, PyClone and SciClone.

108 Across all samples and pipelines, we attempted to execute 5408 subclonal reconstructions. Of these,  
109 4447 (82.2%) successfully completed their execution (**Supplementary Table 2**). Among pipelines  
110 for the single-region subclonal reconstruction of 293 tumours, those using DPCLust achieved the  
111 lowest failure rates (mean  $\pm$  SD:  $1.4\% \pm 1.5\%$ ), followed by those using PhyloWGS ( $2.2\% \pm 1.3\%$ ),  
112 PyClone ( $16.3\% \pm 9.8\%$ ) and SciClone ( $41.2\% \pm 22.4\%$ ; **Supplementary Figure 1A**). The  
113 primary reasons of failure for pipelines using DPCLust and PhyloWGS were excessive memory  
114 requirements (> 250 GB RAM) or run-time (> 3 months). Lack of input SNVs was the largest  
115 failure reason for pipelines using PyClone and SciClone, as PyClone exclusively leverage SNVs  
116 from clonal CNA regions and SciClone utilizes SNVs in copy number neutral regions. Since we

117 used CNA detection tools that identified subclonal variation, in some cases insufficient clonal  
118 CNA regions were available. Post-processing heuristics also contributed to reconstruction failures  
119 across pipelines (**Methods**).

120 Multi-region reconstructions with pipelines using PhyloWGS had the lowest failure rates on the  
121 10 tumours evaluated (mean failure rate  $\pm$  SD: 5.0%  $\pm$  5.5%), followed by PyClone (45.0%  $\pm$   
122 26.6%) and SciClone (93.3%  $\pm$  10.7%; **Supplementary Figure 1B**). Reasons of failure for  
123 pipelines using PhyloWGS include lack of shared CNAs between samples from the same tumour  
124 and prediction of poly-tumour architectures (*i.e.*, multiple independent primary tumours;  
125 **Methods**). PyClone leverages SNVs in clonal CNA regions that are shared between all samples  
126 from the same tumour for multi-region reconstructions and had higher failure rates. Due to similar  
127 requirements for SciClone that all SNVs be in copy number neutral regions and shared between  
128 all samples from the tumour, multi-region reconstructions using SciClone only succeeded in four  
129 cases overall and were excluded from further multi-region reconstruction analyses.

### 130 **Consistency of Subclonal Reconstruction from Single Samples**

131 To evaluate subclonal reconstruction solutions for 293 single region tumours across the four  
132 subclonal reconstruction algorithms, we first compared tumour cellularity (sometimes called  
133 “tumour purity”) estimates across pipelines. Cellularity estimates from CNA detection tools are  
134 inputs to PhyloWGS, PyClone and DPCLust, and as expected predicted cellularity from pipelines  
135 using these algorithms correlated well with those from the CNA detection tool used (TITAN:  
136 0.212–0.623, Battenberg: 0.588–0.876, Spearman’s  $\rho$ ; **Figure 2A-B**). By contrast, SciClone  
137 predicts sample cellularity using orthogonal evidence (VAF of SNVs in copy number neutral  
138 regions). SciClone-estimated cellularity in pipelines using SomaticSniper correlated better with  
139 estimates from CNA detection tools (SomaticSniper-TITAN-SciClone *vs.* TITAN: 0.363,  
140 SomaticSniper-Battenberg-SciClone *vs.* Battenberg: 0.670, Spearman’s  $\rho$ ) than did pipelines using  
141 MuTect (MuTect-TITAN-SciClone *vs.* TITAN: 0.035, MuTect-Battenberg-SciClone *vs.*  
142 Battenberg: 0.358, Spearman’s  $\rho$ ). This suggests that the VAFs of SNVs detected by MuTect have  
143 biased subclone cellular prevalence estimates. Pipeline-estimated cellularity also dropped  
144 dramatically in correlation with CNA detection tool estimated cellularity once the latter reached  
145 0.75 (TITAN: -0.478–(-)0.163, Battenberg: -0.396–(-)0.021, Spearman’s  $\rho$ ). This appears to lead  
146 to the anecdotal observation that high cellularity results from both Battenberg and TITAN could

147 reflect unsuccessful CNA detection, and should be interpreted with caution and perhaps supported  
148 by orthogonal evidence. Finally, Battenberg- and TITAN-estimated cellularity showed poor  
149 correlation (0.271, Spearman's  $\rho$ ). As a result, in 12/12 pipelines using either PhyloWGS, PyClone  
150 or DPCLust, changing the CNA detection tool influenced cellularity estimates more than changing  
151 the SNV detection tool.

152 We next assessed if subclonal reconstruction algorithms differed in the number of subclones they  
153 predict. For each of the 293 tumours evaluated, up to 16 subclonal reconstruction pipelines were  
154 successfully executed, with a median of 14 successful executions. Across samples, a median of  
155 7/16 pipelines agreed on the number of subclones predicted. The median tumour was predicted to  
156 harbor one to three subclones across pipelines, and two randomly selected pipelines would differ  
157 by  $0.9 \pm 0.8$  (mean  $\pm$  SD) in their predicted number of subclones. These variabilities reflect  
158 significant differences between subclonal reconstruction pipelines. No pair of subclonal  
159 reconstruction algorithms consistently produced more similar results across mutation detection  
160 tool combinations. Pipelines using SomaticSniper for SNV detection achieved higher levels of  
161 agreement across subclonal reconstruction algorithms. All four algorithms estimated the same  
162 number of subclones in 59.8% of samples in pipelines using SomaticSniper and Battenberg, and  
163 in 29.3% of samples in those using SomaticSniper and TITAN, though the agreements were largely  
164 driven by concordant monoclonal reconstructions (**Figure 3A-B**). Pipelines using MuTect had  
165 much lower levels of agreement across subclonal reconstruction algorithms (MuTect-Battenberg:  
166 21.5%, MuTect-TITAN: 12.4%; **Figure 3C-D**), although these results suggest pipelines using  
167 SomaticSniper may systematically underestimate subclonal complexity.

168 To better understand the contribution of mutation detection tools to the discordance in predicted  
169 subclonal architectures across pipelines, we compared clonality solutions between pipelines using  
170 the same subclonal reconstruction algorithm across mutation detection tool combinations. There  
171 are strong interactions between mutation detection tools; for example, predictions by the  
172 SomaticSniper-Battenberg-PhyloWGS pipeline agreed poorly with predictions made by other  
173 pipelines using PhyloWGS (**Supplementary Figure 2A**). Agreement was highest between the two  
174 pipelines using MuTect due to the high number of polyclonal solutions. This overall trend was  
175 replicated in pipelines using PyClone, where the SomaticSniper-Battenberg-PyClone pipeline had  
176 high agreement with the SomaticSniper-TITAN-PyClone pipeline but differed from pipelines  
177 using MuTect (**Supplementary Figure 2B**). DPCLust-comprising pipelines using MuTect also

178 predicted high numbers of polyclonal architectures and showed low agreement with other pipelines  
179 (**Supplementary Figure 2C**). Finally, results were similar for pipelines using SciClone, with  
180 pipelines using the same SNV detection tools achieving the highest agreement (**Supplementary**  
181 **Figure 2D**).

182 As PhyloWGS is the only one of the four subclonal reconstruction algorithms evaluated that  
183 predicts the evolutionary relationship between subclones, we compared phylogenetic clone trees  
184 for each sample as predicted by PhyloWGS-comprising pipelines (**Supplementary Figure 3A**).  
185 The most frequently predicted polyclonal architecture was the bi-clonal tree, accounting for  $69.8$   
186  $\pm 25.4\%$  (mean  $\pm$  SD) of polyclonal solutions across pipelines. As multiple phylogenetic clone  
187 trees can be inferred from the same data<sup>2,29</sup>, we evaluated prediction stability across the 2,500  
188 Markov chain Monte Carlo (MCMC) iterations of PhyloWGS after burn-in (**Supplementary**  
189 **Figure 3B-E**). Most samples alternated between  $1.9 \pm 1.2$  (mean  $\pm$  SD) solutions. In 100% of the  
190 cases with an alternative phylogeny, the solution alternated at least once between phylogenetic  
191 clone trees with different numbers of subclones. Further, when PhyloWGS wavered between  
192 solutions that only differed in tree structures (not number of subclones), two alternatives  
193 dominated ( $2.1 \pm 0.3$ , mean  $\pm$  SD). These data suggest that the uncertainty in phylogenetic clone  
194 tree reconstruction comes from the combination of uncertainty from estimating subclone number  
195 and resolving their evolutionary relationships.

196 Taking the consensus across mutation detection tools is a common approach for increasing  
197 confidence in mutation detection<sup>30</sup>. We evaluated how subclonal architectures predicted by  
198 PhyloWGS-comprising pipelines change when using the union and intersection of detected  
199 mutations (**Methods**). Prior to filtering, MuTect detected substantially more unique SNVs than  
200 SomaticSniper (median<sub>Unique SNVs, MuTect</sub> = 5,330, median<sub>Unique SNVs, SomaticSniper</sub> = 627,  $p < 2.2 \times 10^{-16}$ ,  
201 Mann-Whitney U-test; **Supplementary Figure 4A**). Pre-filtering CNAs detected by TITAN and  
202 Battenberg were also substantially imbalanced, with a median of 50.2% and 1.2% of the covered  
203 genome having unique CNAs across samples, respectively ( $p < 2.2 \times 10^{-16}$ , Mann-Whitney U-test;  
204 **Supplementary Figure 4B**). The pipeline using the union of SNVs and the intersect of CNAs  
205 predicted clonality with similar skew to the pipeline using the union of both SNVs and CNAs, and  
206 the pipeline using the intersection of SNVs and union of CNAs predicted clonality with similar  
207 balance to the pipeline using the intersect of both SNVs and CNAs (**Supplementary Figure 4C-**  
208 **F**). This is consistent with our observation that pipeline predictions of complex polyclonal



209 phylogenies using PhyloWGS are primarily driven by large numbers of SNVs detected by MuTect,  
210 and complexity in CNAs has a smaller influence on the delineation of cancer cell populations.

211 Considering the strong influence of SNV detection tools on the number of subclones predicted, we  
212 investigated the VAF and trinucleotide profile of SNVs detected by MuTect and SomaticSniper.  
213 Across all 293 WGS tumour-normal pairs, MuTect-unique SNVs had significantly lower VAFs  
214 than those detected only by SomaticSniper or by both tools ( $\text{median}_{\text{VAF, MuTect-Unique}} = 9.8\%$ ,  
215  $\text{median}_{\text{VAF, SomaticSniper-Unique}} = 24.0\%$ ,  $\text{median}_{\text{VAF, Intersect}} = 28.3\%$ ; both  $p < 2.2 \times 10^{-16}$ , Mann-  
216 Whitney U-test; **Figure 4A**). This supports the finding that predictions of higher numbers of cancer  
217 cell populations is associated with higher numbers of input SNVs with ranging VAFs<sup>15</sup>. SNVs  
218 detected by both tools exhibited a trinucleotide profile characterized by G[C>T]N mutations, while  
219 a higher proportion of SomaticSniper-unique SNVs were [T>C] and MuTect-unique SNVs were  
220 characterized by a high proportion of C>A mutations, especially G[C>A]C and C[C>A]T (**Figure**  
221 **4B-D**). This is suggestive of error profiles related to sequencing or alignment artefacts<sup>31</sup>. As all  
222 raw SNVs detected by SomaticSniper and MuTect were subjected to allow- and deny-list  
223 filtering<sup>13,23</sup> prior to subclonal reconstruction (**Methods**), we also evaluated the effect of filtering  
224 on VAFs and trinucleotide profiles. In general, filtering removed low-VAF SNVs, but minimally  
225 influenced trinucleotide mutational profiles (**Supplementary Figure 5A-E**).

## 226 **Consistency of SNV Clonality**

227 One goal of subclonal reconstruction is to time when individual mutations occurred during tumour  
228 evolution. We therefore compared clonal and subclonal SNV identification for the same set of 293  
229 WGS samples across sixteen pipelines for subclonal reconstruction. As expected from the different  
230 types of SNVs leveraged for subclonal reconstruction, algorithms were highly discordant in the  
231 numbers of SNVs identified as clonal or subclonal. On average, DPCLust used and timed the most  
232 SNVs ( $2,941 \pm 3,929$ , mean  $\pm$  SD; **Figure 5A**), following by PhyloWGS ( $2,473 \pm 1,662$ , **Figure**  
233 **5B**), PyClone ( $1,738 \pm 1,580$ , **Figure 5C**) and SciClone ( $178 \pm 480$ , **Figure 5D**). As expected from  
234 the influence of MuTect on the prediction of subclonal clusters, its use was associated with the  
235 identification of an order of magnitude more subclonal SNVs, but similar numbers of clonal SNVs  
236 as with use of SomaticSniper.

237 To further evaluate how mutation detection tools affect the timing of SNVs, we calculated the  
238 Jaccard index of clonal SNVs identified between all pipeline pairs using the same subclonal

239 reconstruction algorithm, and the same for subclonal SNVs (**Figure 5E**). In PhyloWGS-  
240 comprising pipelines, clonal SNV identifications were in high agreement (mean Jaccard index  $\pm$   
241 SD:  $44.6 \pm 30.2\%$ ) but subclonal SNV identifications were in significantly less agreement in all  
242 samples and pipeline pairs combined ( $10.0 \pm 22.4\%$ ;  $p < 2.2 \times 10^{-16}$ , Wilcoxon signed-rank test),  
243 particularly between pipelines using different SNV detection tools. The results were similar for  
244 other algorithms: DPCLust (clonal Jaccard index:  $46.3 \pm 33.2\%$ , mean  $\pm$  SD; subclonal:  $15.4 \pm$   
245  $27.5\%$ ), PyClone (clonal:  $38.0 \pm 32.2\%$ ; subclonal:  $9.6 \pm 21.6\%$ ) and SciClone (clonal:  $33.3 \pm$   
246  $31.5\%$ ; subclonal:  $14.8 \pm 29.3\%$ ). Overall, we observe diversity in SNV profiles and clonality  
247 predictions across pipelines, with extensive diversity in subclonal SNV profiles associated with  
248 mutation detection tools.

249 To better understand how subclonal reconstruction algorithms differ in their prediction of SNV  
250 clonality, we next focused on SNVs identified as clonal across all pipelines using the same  
251 mutation detection tools. For each sample, we assessed the overlap in clonal SNVs identified by  
252 each pipeline and found only a small percentage of SNVs to be unanimously identified as clonal  
253 per sample: SomaticSniper-TITAN:  $2.0 \pm 5.8\%$ , SomaticSniper-Battenberg:  $3.8 \pm 8.0\%$ , MuTect-  
254 TITAN:  $0.5 \pm 2.0\%$ , MuTect-Battenberg:  $1.0 \pm 3.1\%$  (mean  $\pm$  SD; **Supplementary Figure 6A-**  
255 **D**). Nevertheless, most SNVs were identified as clonal by more than one algorithm  
256 (SomaticSniper-TITAN:  $77.4 \pm 25.2\%$ , SomaticSniper-Battenberg:  $91.9 \pm 17.8\%$ , MuTect-  
257 TITAN:  $48.3 \pm 30.9\%$ , MuTect-Battenberg:  $71.9 \pm 28.5\%$ ). Pipelines using Battenberg were  
258 characterized by large overlaps in clonal SNV identifications between PhyloWGS, DPCLust and  
259 PyClone (SomaticSniper-Battenberg:  $63.2 \pm 34.3\%$ , MuTect-Battenberg:  $46.2 \pm 33.5\%$ ). Pipelines  
260 using TITAN were characterized by modest overlaps between these three, but stronger overlap  
261 between PhyloWGS and DPCLust (SomaticSniper-TITAN:  $42.9 \pm 35.4\%$ , MuTect-TITAN:  $27.1 \pm$   
262  $26.1\%$ ). Given the lack of correlation between subclonal reconstruction algorithms in estimating  
263 subclone number, this could suggest that disagreements between subclonal reconstruction  
264 algorithms mostly fall in defining the subclonal populations.

## 265 **Consistency of CNA Clonality**

266 We also evaluated the influence of mutation detection tools on clonal and subclonal CNA  
267 identification. We focused on PhyloWGS, as it was the only algorithm considered here that co-  
268 clusters SNVs and CNAs. Previous work on this cohort using the SomaticSniper-TITAN-

269 PhyloWGS pipeline identified four clonal CNA subtypes and three subclonal CNA subtypes<sup>13</sup>, so  
270 we first evaluated their robustness across pipelines. In general, clonal subtypes were robust to  
271 pipeline changes, while subclonal subtypes were less so (**Supplementary Figure 7A-B,**  
272 **Supplementary Table 3**). Pipelines employing the same CNA detection tool also had more similar  
273 profiles than those using different ones.

274 We next assessed the agreement of these pipelines in their identification of clonal and subclonal  
275 CNAs. We calculated the Jaccard index of 1.0 Mbp genomic bins with CNAs between pipeline  
276 pairs, where the direction of aberration (*i.e.*, gain *vs.* loss) was considered. We found significantly  
277 greater agreement for clonal CNAs compared to subclonal CNAs in comparisons between every  
278 pipeline pair (mean clonal Jaccard index  $\pm$  SD:  $50.5 \pm 21.1\%$ , subclonal Jaccard:  $15.6 \pm 21.8\%$ ;  
279 all  $p < 2.2 \times 10^{-16}$ , Wilcoxon signed-rank test; **Supplementary Figure 7C**). Pipelines using the  
280 same CNA detection tool tended to agree, although divergence was expected because the  
281 reconstructed clonality of CNA segments can be influenced by the VAFs of SNVs in the segment.  
282 By contrast, pipelines with different CNA detection tools had less clonal and little subclonal  
283 agreement. Thus, for both SNVs and CNAs, clonal mutational landscapes were relatively invariant  
284 to pipeline but subclonal ones were not.

## 285 **Impact of Reconstruction Variability on Downstream Analyses**

286 Given these differences in SNV and CNA clonality prediction across pipelines, we sought to  
287 understand how they might influence the timing of mutations in cancer driver genes. These genes  
288 are of particular relevance as they can be actionable as predictive or prognostic biomarkers. We  
289 examined the clonality of mutations in five genes driven by recurrent somatic SNVs (*ATM,*  
290 *FOXA1, MED12, SPOP* and *TP53*) and eight driven by recurrent somatic CNAs (*CDHI,*  
291 *CDKN1B, CHD1, MYC, NKX3-1, PTEN, RBI* and *TP53*) in localized prostate cancer<sup>13,23</sup>. Focusing  
292 on PhyloWGS-comprising pipelines, these driver events were overwhelmingly predicted to occur  
293 early (*i.e.* clonally) during tumour evolution, with  $87.2 \pm 16.8\%$  (mean  $\pm$  SD) of SNV and  $91.5 \pm$   
294  $6.4\%$  of CNA driver mutations identified as clonal across pipelines (**Supplementary Figure 8A-**  
295 **B**). There was also broad consensus in these predictions: when a clonal SNV was identified by any  
296 single pipeline in a specific driver gene and sample, all four pipelines identified a clonal SNV in  
297 that driver gene in the same sample in  $39.5 \pm 22.5\%$  of cases (mean  $\pm$  SD). CNAs showed even  
298 higher consensus ( $50.4 \pm 14.8\%$ ; **Supplementary Figure 8C**). One outlier was *MED12*, where

299 there was disagreement across pipelines with the same SNV detection tools: since *MED12* is  
300 located on the X chromosome and Battenberg does not generate copy number status for regions of  
301 uncertainty and the sex chromosomes, its mutations were disregarded during subclonal  
302 reconstruction because PhyloWGS only considers SNVs with overlapping copy number status.

303 We then evaluated how CNA clonality predictions affect the identification of genes that are  
304 significantly differentially mutated clonally vs. subclonally. Within each pipeline we determined  
305 whether each 1.0 Mbp genomic bin had different proportions of gains and losses clonally and  
306 subclonally (FDR < 0.05, Pearson's  $\chi^2$  Test, clonal: loss, neutral, gain vs. subclonal: loss, neutral,  
307 gain; **Methods**). The number of genes in regions with CNAs occurring statistically more  
308 frequently early or late differed dramatically across PhyloWGS-comprising pipelines (MuTect-  
309 TITAN: 5,344; SomaticSniper-TITAN: 5,198; MuTect-Battenberg: 1,498; SomaticSniper-  
310 Battenberg: 339). A consensus set of 339 genes showed a bias in timing in all pipelines as  
311 preferentially mutated clonally (**Supplementary Figure 9A, Supplementary Table 4**). These  
312 genes were enriched for *TP53*-based regulation of death receptors, *TRAIL* signaling and natural  
313 killer cell mediated cytotoxicity (FDR < 0.05; **Supplementary Figure 9B**).

314 To evaluate whether pipeline differences could influence the accuracy of biomarkers, we focused  
315 on biochemical relapse after definitive local therapy. Previous work has identified clonality to be  
316 prognostic in this setting, both independently and when combined with an established multi-modal  
317 (CNA, SNV, SV and methylation) gene-specific biomarker<sup>13,23</sup>. Discretization by clonality  
318 (monoclonal vs. polyclonal) only stratified patients by outcome in the SomaticSniper-TITAN-  
319 PhyloWGS pipeline ( $p = 0.004$ , log-rank test; **Supplementary Figure 10A**), but not any other (all  
320  $p > 0.05$ , log-rank test; **Supplementary Figure 10B-P**). The unified biomarker integrating  
321 clonality and a multi-modal biomarker achieved prognostic value in more pipelines ( $p < 0.05$  in  
322 14/16 models, log-rank test; **Supplementary Figure 11A-P**), with concordant trends across all  
323 pipelines. Thus, the prognostic effect size of clonality in prostate cancer is smaller than the  
324 technological effect size in this cohort, with a clinical signal smaller than technical variance. As a  
325 result, the translational potential of clonality in localized prostate cancer is improved when it is  
326 integrated with complementary gene-specific biomarker information.

## 327 **Comparing Reconstructions using Single and Multiple Regions**

328 Our analyses of a large cohort of single-sample reconstructions highlight large inter-pipeline  
329 differences in the **determination of subclonal architecture and prediction of mutation clonality**. To  
330 better **relate** these results to **the** ground-truth, we focused on a set of ten localized prostate cancers  
331 where samples from multiple regions of the tumour were available (30 genomes in total, ranging  
332 from 2-4 per **patient**). These data allowed us to directly compare single-region to multi-region  
333 reconstructions using PhyloWGS **and PyClone**, providing an estimate of the extent to which the  
334 former underestimates true clonal complexity.

335 **We first** quantified the differences in the number of subclones **predicted** from single-region and  
336 multi-region reconstructions of the **ten** tumours (**Supplementary Table 5**). Multi-region  
337 reconstructions **predicted** more subclones than single-region reconstructions **in pipelines using**  
338 **PhyloWGS**:  $4.6 \pm 2.4$  (mean  $\pm$  SD) subclones were **predicted** with multi-region reconstructions  
339 while  $2.0 \pm 0.9$  subclones were **predicted** with single-region reconstructions (**Figure 6A**). This  
340 difference was not seen in pipelines using PyClone (multi-region reconstructions:  $2.2 \pm 1.7$ , single-  
341 region reconstructions:  $2.3 \pm 2.0$ ), likely due to the constraint that only mutations present in all  
342 samples are used for multi-region reconstruction (**Figure 7A**). These data suggest that the typical  
343 single-sample reconstruction **identifies fewer** than half of the subclones present in the tumour, **and**  
344 **this could very well be a lower-bound estimate** because of the limited sequence depth and spatial  
345 **sampling of this cohort**. On the other hand, multi-sample reconstructions also **predicted**  
346 significantly more subclones within the index lesion sample compared to single-sample  
347 reconstruction of the index lesion **in pipelines using PhyloWGS** ( $p = 2.4 \times 10^{-4}$ , Wilcoxon signed-  
348 rank test; **Supplementary Figure 12A**), but not those using PyClone ( $p \approx 1$ , Wilcoxon signed-  
349 rank test; **Supplementary Figure 12B**). Together this suggests that single-region reconstructions  
350 are limited by spatial sampling from fully resolving the intra-tumoural heterogeneity of both the  
351 overall tumour and the sampled region, for example due to cases where subclones appear with the  
352 same CCF and are thus indistinguishable from single-region reconstructions alone<sup>32</sup>.

353 We next sought to determine the extent of variability in SNV clonality predictions between single-  
354 region and multi-region reconstructions. We identified SNVs that were **predicted be the same**  
355 **clonality (clonal or subclonal) in both single- and multi-region reconstructions** ('Match in Multi  
356 and Single'). For SNVs with mismatched clonality, we further categorized them as clonal in multi-

357 region reconstruction and subclonal in single-region reconstruction ('Clonal in Multi-region') or  
358 *vice versa* ('Subclonal in Multi-Region'), or SNVs that were uniquely considered in single-region  
359 reconstructions ('Unique in Single-region') or multi-region reconstructions ('Unique in Multi-  
360 region'). The last category of SNVs is unique to PhyloWGS as it is able to consider SNVs unique  
361 to individual samples for multi-region analysis. SNV clonality predictions matched less than half  
362 the time for pipelines using PhyloWGS ( $31.9 \pm 24.6\%$ , mean  $\pm$  SD; **Figure 6B**). Pipelines using  
363 PyClone achieved modestly higher clonality agreement, perhaps due to the smaller number of  
364 subclones predicted in multi-region reconstructions and the lack of multi-region unique SNVs  
365 ( $38.6 \pm 28.4\%$ ; **Figure 7B**). Mismatched SNVs tended to be clonal in single-region reconstructions  
366 and subclonal in multi-region reconstructions, as expected. Consistent with simulations<sup>33</sup> and  
367 previous observations, multi-region reconstructions are able to better define subclonal populations  
368 of cells by identifying and disambiguating those missed or merged by single-region sampling.

369 We also examined the agreement between single-region and multi-region reconstruction CNA  
370 clonality predictions in pipelines using PhyloWGS (**Figure 6C**). Agreements were similarly  
371 variable, with less than half of CNAs matching in clonality between the single- and multi-region  
372 reconstructions and extensive variance across samples ( $33.6 \pm 31.7\%$ , mean  $\pm$  SD). As with SNVs,  
373 mismatches mostly involved clonal CNAs in single-region reconstructions identified as subclonal  
374 in multi-region reconstructions.

375 To better understand this sampling bias, we analyzed how well the clonal population of the index  
376 lesion from single-region reconstruction represents the clonal population of the entire tumour. In  
377 PhyloWGS-comprising pipelines, multi-region reconstruction often showed that SNVs identified  
378 as clonal in the index lesion were actually subclonal (**Supplementary Figure 13A**). Nevertheless,  
379 the majority of single-region clonal SNVs were truly clonal in multi-region reconstruction ( $66.6 \pm$   
380  $29.8\%$ , mean  $\pm$  SD). As before, pipelines using PyClone showed much higher agreement ( $91.4 \pm$   
381  $23.3\%$ ), likely because of the large number of excluded SNVs (**Supplementary Figure 13B**). A  
382 similar analysis of subclonal SNVs showed that most subclonal SNVs defined by single-region  
383 reconstructions of the index lesion are subclonal in multi-region reconstructions in pipelines using  
384 PhyloWGS and MuTect ( $12.2 \pm 17.5\%$ , mean  $\pm$  SD). In contrast, multi-region reconstruction  
385 pipelines using PhyloWGS and SomaticSniper predicted many subclonal SNVs from single-region  
386 reconstructions as clonal instead ( $55.2 \pm 40.3\%$ ). This highlights a potential limitation of multi-  
387 region subclonal reconstruction algorithms with a need for shared SNVs or CNAs.

## 388 Discussion

389 It is difficult to benchmark the accuracy of subclonal **reconstruction** methodologies since a **robust**  
390 gold-standard experimental dataset **does not yet exist**. Simulation frameworks are of great value,  
391 but **might not** fully recapitulate the error-profiles and signal-biases of real data<sup>34</sup>. **To evaluate the**  
392 **technological variability in estimating aspects of** subclonal architectures, **we evaluated** 293  
393 tumours using **sixteen** pipelines. These data provide **an** experimental lower-bound on the  
394 algorithmic variability of tumour subclonal reconstruction in a large high-depth whole-genome  
395 sequencing cohort, **at least for a single cancer type and stage**. We complement these data by  
396 assessing **eighteen** subclonal reconstruction pipelines across a set of 10 multi-region tumours **to**  
397 estimate the degree to which single-sample reconstructions underestimate clonal complexity **the**  
398 **full tumour**.

399 **Subclonal reconstruction algorithms differ substantially in their prediction of subclonal**  
400 **architecture across all mutation detection tool combinations, with no pair of algorithms**  
401 **consistently achieving similar results in cellularity estimates, prediction of subclone number and**  
402 **assignment of mutation clonality. While the subclonal CNA detection tool used mostly influenced**  
403 **cellularity estimates but no other aspects of subclonal architecture, large differences were driven**  
404 **by changing the SNV detection approach. Differences between SNV detection tools led to major**  
405 **divergences in subclonal reconstruction: pipelines using MuTect found extensive subclonal**  
406 **diversity, at least partly due to the greater number of low VAF mutations detected. SNV detection**  
407 **benchmarking efforts<sup>31</sup> could aid in the further characterization of the error profiles of SNV**  
408 **detection tools and optimize parameter tuning to improve subclonal reconstruction. Future studies**  
409 **might benefit from merging multiple subclonal reconstruction pipelines, for example to provide a**  
410 **potential envelope of upper and lower bounds on different features of the reconstruction.**

411 **The potential translational and clinical impact of these technical variabilities is considerable. For**  
412 **example, technological differences between analysis pipelines were larger than the effect-size of**  
413 **the association between evolutionary complexity and patient survival. This suggests that estimates**  
414 **of technical variability should be provided for analyses dependent on subclonal architecture, such**  
415 **as in studies mapping evolutionary and migration trajectories between primary and metastatic**  
416 **tumours. Studies identifying clonal and especially subclonal driver mutations should be interpreted**  
417 **with such variability estimates for reference as subclonal mutational landscapes were found to be**

418 especially vulnerable to pipelines changes when clonal ones were less so. Articulating how these  
419 algorithmic differences relate to the clinical effect-size will greatly improve interpretability of  
420 these types of data.

421 Future studies also need to carefully consider the failure-rates of different reconstruction  
422 algorithms, as algorithms leveraging clonal or neutral copy number regions might not be suitable  
423 for tumour types characterized by large numbers of CNAs and might call for specific CNA  
424 detection strategies. Computational failures are problematic for clinical applications and, in  
425 combination with the substantive computational requirements that scale with the number of  
426 mutations, could be problematic for cancer types characterized by a high mutational burden.

427 Our evaluation of subclonal reconstruction using data from spatially distinct regions of tumours  
428 found that reconstructions relying on a single sample systematically underestimated the number of  
429 subclones in a tumour. Input constraints and non-exhaustive sequencing depth and spatial sampling  
430 in multi-region reconstructions also suggest that the current level of underestimation is only the  
431 lower-bound. This is in line with previous work in kidney cancer<sup>6,11</sup>. These data also agree with  
432 previous work showing the distinct mutational profiles of prostate cancer samples from spatially  
433 distinct regions of the same tumour<sup>8</sup> and reinforces the hypothesis that sufficient sampling will  
434 uncover multiple subclones in nearly all cancers. It also suggests that strategies for robust multi-  
435 region-aware subclonal mutation detection would be a significant benefit to subclonal  
436 reconstruction analyses.

437 Larger datasets are necessary to better evaluate the performance of subclonal reconstruction  
438 methodologies. While simulated data is valuable<sup>34</sup>, single-cell sequencing datasets will likely  
439 significantly improve the evaluation of ground truth for subclonal reconstruction algorithms in  
440 patient samples. In the meantime, this work involving a large clinical cohort will aid in refining  
441 subclonal reconstruction methods and provide guidance for evaluating the subclonal architecture  
442 of cancer samples.

443



## 444 **Methods**

### 445 **Patient Cohort**

446 We aggregated a retrospective cohort of localized prostate tumours with patient consent and  
447 Research Ethics Board approval from published datasets, with whole-genome sequencing of  
448 tumour samples and matched blood-based normal samples<sup>13,23,24,35–38</sup>. The cohort includes 293  
449 patients with tumour samples from the index lesion and 10 patients with multiple samples from  
450 intraductal carcinoma and juxtaposed adjacent invasive carcinoma. For patients receiving  
451 radiotherapy, the index tumour was identified on transrectal ultrasound and sampled by needle  
452 biopsies (TRUS-Bx) and was deemed the largest focus of disease that was confirmed  
453 pathologically. A fresh-frozen needle core ultrasound-guided biopsy to this index lesion was  
454 obtained for macro-dissection. For patients receiving surgery, the index tumour was identified  
455 macroscopically by a GU expert pathologist at the point of surgery and later sampled and  
456 biobanked. A fresh-frozen tissue specimen from the index lesion was then obtained from macro-  
457 dissection. Details of the patient cohort have been described previously<sup>13,24</sup>.

458 We focused on patients with clinical intermediate-risk disease as defined by NCCN, with  
459 intermediate-risk factors (T2b or T2c disease, ISUP Grade Group 2 or 3 or pre-treatment prostate  
460 specific antigen (PSA) serum levels between 10-20 ng/mL). All patients received either precision  
461 image-guided radiotherapy or radical prostatectomy with no randomization or classification and  
462 were hormone naive at time of therapy. Four patients in the multi-region sequencing cohort carried  
463 germline BRCA2 mutations and had formalin-fixed paraffin-embedded tissues instead of fresh-  
464 frozen. Sample regions suitable for micro-dissection (tumour cellularity > 70%) were marked by  
465 genitourinary pathologists and manually macro-dissected, followed by DNA extraction and  
466 sequencing.

### 467 **Whole genome sequencing data analysis**

468 Protocols for whole-genome sequencing data generation and processing have been previously  
469 described<sup>13,23,24</sup>. Briefly, raw sequencing reads from the tumour and normal samples were aligned  
470 against human reference genome build hg19 using bwa-aln (v0.5.7)<sup>39</sup>. Lane-level BAMs from the  
471 same library were merged and duplicates were marked using picard (v1.92). Local realignment  
472 and base quality recalibration were performed together for tumour/normal pairs using GATK  
473 (v.2.4.9)<sup>40</sup>. Tumour and normal sample-level BAMs were extracted separately, had headers

474 corrected with SAMtools (v0.1.9)<sup>41</sup> and were indexed with picard (v1.107). ContEst  
475 (v1.0.24530)<sup>42</sup> was used to estimate lane-level and sample-level sample mix-up and lane-level  
476 cross-individual contamination on all sequences, with no significant contaminated detected.

## 477 **Tumour Somatic Mutation Assessment**

478 We **detected** subclonal copy number aberrations from whole-genome sequencing data using  
479 Battenberg (v2.2.6)<sup>7</sup>, TITAN (v1.11.0)<sup>25</sup> and FACETS (v0.5.14)<sup>28</sup>. First, Battenberg (v2.2.6) was  
480 installed with underlying ASCAT (v2.5)<sup>43</sup> using the installation and running wrapper  
481 cgpBattenberg (v3.1.0). Required reference files were downloaded as instructed in  
482 <https://github.com/Wedge-Oxford/battenberg> and further required data files were generated as  
483 instructed in <https://github.com/cancerit/cgpBattenberg>. An ignore file was created for the genome  
484 assembly hg19 to exclude all chromosomes not in 1-22. Battenberg (v2.2.6) was run with -gender  
485 of XY for male patients and -t of 14 to run using 14 threads, and otherwise default parameters. The  
486 resulting primary solution was subjected to manual refitting in situations meeting the following  
487 criteria: 1) the solution involved a high copy number segment with high BAF and low logR,  
488 indicating an unrecognized homozygous loss event, 2) nearly all copy number **aberrations** were  
489 subclonal, 3) there were unreasonably high copy numbers up to infinity. Refitting was performed  
490 until the concerns for refitting were resolved or for three attempts after which the original solution  
491 was accepted. The CNAs obtained from the primary solution, along with tumour cellularity and  
492 ploidy were used for further analysis. We have described subclonal copy number analysis using  
493 TITAN (v1.11.0) previously in detail<sup>13</sup>. Briefly, TITAN (v1.11.0) was run through the Kronos  
494 (v1.12.0)<sup>44</sup> pipeline for whole-genome sequence preprocessing and subclonal copy number  
495 assessment. GC and mappability files for bias correction were prepared using HMMcopy  
496 (v0.1.1)<sup>45</sup> and bowtie (v2.2.6)<sup>46</sup> on the hg19 reference genome. Heterogeneous positions in the  
497 sequence data were identified by MutationSeq (v4.3.7)<sup>47</sup> using known dbSNP sites from GATK  
498 (v2.4.9). For each whole-genome sequence, TITAN (v1.11.0) made predictions of the existence of  
499 one to five subclones based on the given input numClusters and the solution with the lowest  
500 S\_Dbw validity index<sup>25</sup> was used to obtain the cellularity, ploidy and subclonal CNAs for  
501 downstream analysis. **Finally, to prepare inputs for subclonal copy number assessment by**  
502 **FACETS (v0.5.14), the accompanying snp-pileup (v434b5ce) algorithm was installed with**  
503 **underlying htlib (v1.9)<sup>41</sup>. A SNP location VCF file was downloaded as instructed for hg19 with**  
504 **SNP version b151 and human genome build version GrCh37p13 from**

505 [ftp://ftp.ncbi.nlm.nih.gov/snp/organisms/human\\_9606\\_b151\\_GRCh37p13/VCF/00-](ftp://ftp.ncbi.nlm.nih.gov/snp/organisms/human_9606_b151_GRCh37p13/VCF/00-common_all.vcf.gz)  
506 [common\\_all.vcf.gz](ftp://ftp.ncbi.nlm.nih.gov/snp/organisms/human_9606_b151_GRCh37p13/VCF/00-common_all.vcf.gz), and [snp-pileup \(v434b5ce\)](ftp://ftp.ncbi.nlm.nih.gov/snp/organisms/human_9606_b151_GRCh37p13/VCF/00-snp-pileup.vcf.gz) was run using developer recommended parameters  
507 (-g -q15 -Q20 -P100 -r25,0). All FACETS (v0.5.14) runs used the seed 1234 and default  
508 parameters for all steps, except for [procSample](#) where the developer recommended parameter `cval`  
509 = 150 was used.

510 We used MuTect (v1.1.4)<sup>27</sup> and SomaticSniper (v1.0.2)<sup>26</sup> for the **detection** of somatic single  
511 nucleotide variants from whole-genome sequencing data. MuTect was run to obtain candidate  
512 SNVs with dbSNP138<sup>48</sup>, COSMIC (v66)<sup>49</sup> and default parameters except the `-tumor_lod` option  
513 (tumor limit of detection). The `-tumor_lod` option was set to 10 to increase the stringency of  
514 detection. Outputs that contained REJECT were filtered out and the remaining SNVs were used  
515 for downstream analysis. Details for SomaticSniper (v1.0.2) variant **detection** have been described  
516 previously<sup>23</sup>. In short, SomaticSniper (v1.0.2) was used to identify candidate SNVs with default  
517 parameters except the `-q` option (mapping quality threshold), which was set to 1 as per developer  
518 recommendation. Candidate SNVs were filtered through standard and LOH filtering using a pileup  
519 indel file generated on the sequence data using SAMtools (v0.1.9)<sup>41</sup>, bam-readcount filtering and  
520 false positive filtering. Only high confidence somatic SNVs obtained from the high confidence  
521 filter using default parameters were used for further analysis, **as per developer recommendations**.  
522 **We further** performed annotation and filtering on all SNVs, with full details given previously<sup>13</sup>. In  
523 brief, SNVs obtained by MuTect (v1.1.4) and SomaticSniper (v1.0.2) were annotated with  
524 associated genes and functions by ANNOVAR (v2015-06-17)<sup>50</sup> using RefGene, subjected to **deny-**  
525 **list** filtering to remove known germline contaminants and sequencing artifacts and **allow-list**  
526 filtering through COSMIC (v70)<sup>49</sup>. This was done before downstream subclonal reconstruction.  
527 SNVs were further subjected to filtering to remove SNVs not at callable bases (where callable  
528 bases are those with  $\geq 17x$  coverage for the tumour and  $\geq 10x$  coverage for the normal).

## 529 **Subclonal Reconstruction Pipeline Construction**

530 We define a subclonal reconstruction pipeline as comprised of a SNV detection tool, a CNA  
531 detection tool and a subclonal reconstruction algorithm. A pipeline is said to be using or  
532 comprising of a tool and/or an algorithm when the tool/algorithm is incorporated as one step of the  
533 pipeline.

534 For single-region reconstruction, the SNV detection tools SomaticSniper (v1.0.2) and MuTect  
535 (v1.1.4), the CNA detection tools Battenberg (v2.2.6) and TITAN (v1.11.0), and the subclonal  
536 reconstruction algorithms PhyloWGS (v3b75ba9), PyClone (v0.13.0), DPCLust (v2.2.5) and  
537 SciClone (v1.0.7) were combined in factorial combinations to construct 16 pipelines. Subclonal  
538 reconstruction was run on the cohort of 293 tumours with index lesion sequencing for single-region  
539 subclonal reconstruction.

540 For multi-region reconstruction, the SNV detection tools SomaticSniper (v1.0.2) and MuTect  
541 (v1.1.4), the CNA detection tools Battenberg (v2.2.6), TITAN (v1.11.0) and FACETS (v0.5.14),  
542 and the subclonal reconstruction algorithms PhyloWGS (v3b75ba9), PyClone (v0.13.0) and  
543 SciClone (v1.0.7) were combined in factorial combinations to construct 18 pipelines. For the 10  
544 tumours with multi-region sequencing, each individual sequencing sample (total 30, 2-4 samples  
545 per tumour) was first subjected to single-region subclonal reconstruction using the 18 pipelines,  
546 followed by multi-region subclonal reconstruction using the 18 pipelines where all regions of a  
547 tumour were provided as input.

## 548 **Subclonal Reconstruction of Tumours using PhyloWGS**

549 We used the `cnv-int` branch of PhyloWGS (<https://github.com/morrislab/phyloWGS/tree/cnvint>,  
550 commit: 3b75ba9c40cfb27ef38013b08f9e089fa4efa0c0)<sup>15</sup> for the reconstruction of tumour  
551 phylogenies, as described previously<sup>13</sup>. Briefly, subclonal CNA segments and **cellularity inputs**  
552 were parsed using the provided `parse_cnvs.py` script (the `parse_cnvs.py` was custom augmented to  
553 **process inputs from FACETS [v0.5.14]**) and filtered to remove any segments shorter than 10 kbp.  
554 The `create_phyloWGS_inputs.py` script was used to generate PhyloWGS (v3b75ba9) inputs for each  
555 sample. All default parameters were used, including limiting the number of SNVs considered to  
556 5,000 for the interest of runtime to launch reconstructions using `evolve.py`. Multi-region subclonal  
557 reconstruction was performed by providing all regions belonging to the same tumour as input for  
558 the reconstruction and the procedure was otherwise identical to the single-region reconstructions.

559 The best **phylogenetic clone** tree for each run and the CNAs and SNVs associated with each  
560 subclone in that structure were determined by parsing the output JSON files for the tree with the  
561 largest log likelihood value. In addition to the best tree structure, the output JSON file was also  
562 parsed for all predicted tree structures as ordered by log likelihood values to assess the change in  
563 predictions across the 2,500 Markov chain Monte Carlo iterations.

## 564 **Subclonal Reconstruction of Tumours using PyClone**

565 We used PyClone (v0.13.0)<sup>17</sup> for single- and multi-region mutation clustering. A mutation input  
566 file was created for each sample by obtaining the tumour reference and variant read counts for  
567 each SNV from input VCFs and annotating them with the clonal major and minor copy numbers  
568 for the position from CNA inputs. Since PyClone (v0.13.0) leverages SNVs in clonal CNA  
569 regions, all SNVs in subclonal CNA regions were not considered. SNVs in regions without copy  
570 number information were also discarded, and the normal copy number was set to 2 for autosomes  
571 and 1 for chromosomes X and Y. The mutation input file, along with tumour cellularity as  
572 predicted by the subclonal CNA detection tool were used as inputs for the `run_analysis_pipeline`  
573 to launch PyClone (v0.13.0)<sup>17</sup>, using 12345 as the seed for all runs. Notably, since PyClone  
574 (v0.13.0) was originally developed for deep sequencing (>100x) data, the developer recommended  
575 setting the “density” parameter to “pyclone\_binomial” to account for characteristics whole-  
576 genome sequencing data. The number of Markov chain Monte Carlo iterations were also set to  
577 100,000, with 1,000 burn-ins. Otherwise default parameters were used. PyClone (v0.13.0)  
578 outputted ‘cellular prevalence’ as defined by the authors as ‘the proportion of tumor cells harboring  
579 a mutation’ fits the definition of cancer cell fraction for this study, and cellular prevalence as  
580 defined in this study was calculated by multiplying the outputted ‘cellular prevalence’ with purity  
581 estimates from the respective CNA detection tool. Multi-region reconstructions using PyClone  
582 (v0.13.0) were launched by including all mutation input files and tumour cellularities prepared for  
583 single-region reconstructions as outlined above for all samples of a tumour as input to  
584 `run_analysis_pipeline`. Cellular prevalence as defined in this study was similarly obtained from  
585 ‘cellular prevalence’ as outputted by PyClone (v0.13.0) by individually adjusting for the tumour  
586 contents for each sample of the tumour.

## 587 **Subclonal Reconstruction of Tumours using DPCLust**

588 We used DPCLust (v2.2.5)<sup>16</sup> for single-region subclonal reconstruction. DPCLust (v2.2.5) was run  
589 using the `dpc.R` pipeline available *via* the DPCLust SMC-HET Docker ([https://github.com/Wedge-](https://github.com/Wedge-Oxford/dpclust_smchet_docker)  
590 [Oxford/dpclust\\_smchet\\_docker](https://github.com/Wedge-Oxford/dpclust_smchet_docker), commit a1ef254), using also `dpclust3p` (v1.0.6). The pipeline was  
591 customized to process inputs from SomaticSniper (v.1.0.2) and TITAN (v1.11.0). The inputs for  
592 each tumour sample were the VCF file provided by the SNV detection tool, and subclonal copy  
593 number, cellularity, ploidy, and purity as predicted by the subclonal CNA detection tool, using  
594 12345 as the seed and otherwise default parameters. The results in the `subchallenge1C.txt` output

595 file were taken as the mutation clustering solution to obtain the number of subclones predicted by  
596 DPCLust and their cellular prevalence (v2.2.5)<sup>16</sup>. Results in the subchallenge2A.txt output file were  
597 taken to define the mutation composition of each cluster.

## 598 **Subclonal Reconstruction of Tumours using SciClone**

599 We used SciClone (v1.0.7)<sup>20</sup> for single- and multi-region subclonal reconstruction. Input VCFs  
600 were used to calculate variant allele frequencies (in percentage) and CNA inputs were used to  
601 determine regions with loss of heterozygosity. Only SNVs in copy number neutral (major = 1,  
602 minor = 1) regions were considered by SciClone (v1.0.7) and all samples were run using default  
603 parameters. Multi-region reconstructions using SciClone (v1.0.7) were run by including inputs for  
604 all samples of a tumour. Mutation clusters defined by SciClone (v1.0.7) were characterized using  
605 variant allele frequencies, and their VAFs were multiplied by a factor of 2 to convert to cellular  
606 prevalence as defined in this study.

## 607 **Post Processing of Subclonal Reconstruction Solutions**

608 Since subclones in PhyloWGS (v3b75ba9) trees are numbered based on cellular prevalence instead  
609 of evolutionary relationship, trees were transformed to consistent representations to allow  
610 comparison across cohorts following two rules: 1) trees are left-heavy, 2) all nodes at a particular  
611 tree depth must have numbers greater than that of nodes at lower tree depths, with the root node  
612 (normal cell population) starting at 0. Further, pruning of nodes was performed following the  
613 heuristic that each node must have at least 5 SNVs or 5 CNAs and a **minimum** cellular prevalence  
614 of 10%, creating a subclonal diversity lower bound for each tumour<sup>13</sup>. A node was **pruned and**  
615 **merged** with its sibling if **their cellular prevalence difference** was  $\leq 2\%$  and if both were driven  
616 **purely by SNVs (had  $\leq 5$  CNAs)**. A node was merged with its parent node if **their cellular**  
617 **prevalence difference** was  $\leq 2\%$ . When PhyloWGS (v3b75ba9) produced a **poly-tumour** solution  
618 for the best consensus tree, the algorithm was re-run up to 12 times with different random number  
619 generator seeds after which the final **poly-tumour** solution was accepted and **considered to be a**  
620 **reconstruction failure**. The seeds were applied in the following order: 12345, 123456, 1234567,  
621 12345678, 123456789, 246810, 493620, 987240, 1974480, 3948960, 7897920 and 15795840. In  
622 the event PhyloWGS (v3b75ba9) failed to produce a solution due to reconstruction failures or  
623 excessive runtime ( $>3$  months), the sample was excluded from analysis for that pipeline.

624 PyClone (v0.13.0), DPCLust (v2.2.5) and SciClone (v1.0.7) identified subclonal populations were  
625 pruned using similar heuristic as that for PhyloWGS (v3b75ba9). Specifically, for each tumour  
626 sample, a mutation cluster was pruned if it had fewer than five supporting SNVs or a cellular  
627 prevalence below 10% if it is the clonal cluster or below 2% if it is a subclonal cluster. If there  
628 were less than 5 total mutations (SNVs) assigned to clusters in a sample, or if all clusters had  
629 cellular prevalence of below 10%, a failed reconstruction was designated to the sample. Otherwise  
630 pruned clusters were merged with their nearest neighbor in cellular prevalence, and the weighted  
631 mean of cellular prevalence was assigned to the merged node. Moreover, two clusters were merged  
632 if they differed in cellular prevalence by  $\leq 2\%$ . Finally, mutation clusters were ordered by  
633 decreasing cellular prevalence and renumbered accordingly, and the cluster with the highest  
634 cellular prevalence was treated as the clonal cluster and its cellular prevalence taken as the  
635 cellularity estimated by the pipeline. This was a conservative approach as the detection of multiple  
636 primary tumours is challenging from single-sample subclonal reconstruction<sup>13</sup>.

### 637 **Union and Intersection of Mutation Detection Tools**

638 We obtained the union and intersection of raw SNVs by SomaticSniper (v1.0.2) and MuTect  
639 (v1.1.4) for each tumour sample using vcf-isec of vcftools (v0.1.15). The union and intersection  
640 sets of SNVs were then annotated and filtered with the same method as described above before  
641 being used in subsequent analysis<sup>13</sup>. For the comparison of mutation characteristics as detected by  
642 MuTect (v1.1.4) and SomaticSniper (v1.0.2), all SNVs detected by each tool across all 293 index  
643 lesion samples were pooled to assess their VAFs and trinucleotide contexts. SNVs were grouped  
644 as intersect if detected by both tools, or as MuTect-unique or SomaticSniper-unique, both pre- and  
645 post-filtering. The effect of filtering was assessed by comparing SNVs retained after filtering  
646 ('SomaticSniper' and 'MuTect') with those removed by it ('Removed SomaticSniper' and  
647 'Removed MuTect'). Trinucleotide context profiles for each group of SNVs were normalized by  
648 the expected number of each trinucleotide across the hg19 genome.

649 We determined the union and intersection of CNAs detected by TITAN (v1.11.0) and Battenberg  
650 (v2.2.6), first parsed using parse\_cnvs.py script of PhyloWGS (v3b75ba9) for consistent  
651 formatting, on a per base-pair basis. The intersection of CNAs, based on genomic coordinates and  
652 major and minor copy number, was determined using the GenomicRanges (v1.28.6)<sup>51</sup> package in  
653 R (v3.2.5). Regions with disagreeing copy number were identified using bedtools (v2.27.1)<sup>52</sup> and

654 bedr (v1.0.6)<sup>53</sup>. A region is defined to have a tool-unique CNA if one tool detected a copy number  
655 aberration for the region while the other identified it as copy number neutral (major and minor  
656 copy number of 1). Regions where both algorithms detected different copy number aberrations were  
657 classified as disagreements. The union set of CNAs thus contained the intersection of CNAs and  
658 CNAs unique to either tool, and regions of disagreement were excluded as there was no natural  
659 way to resolve discrepancies. In contrast to TITAN, when a region is determined to have a  
660 subclonal aberration, Battenberg (v2.2.6) produces two entries, a clonal and subclonal copy  
661 number for each genomic region. These regions were labelled Battenberg-unique for its clear  
662 delineation of subclonal CNAs. However, the TITAN (v.1.11.0) copy number aberration result for  
663 the region (if any) is used in the union of CNAs to avoid conflicting CNAs in the same region, as  
664 one cannot combine clonal Battenberg (v2.2.6) results with TITAN (v1.11.0) aberrations. The  
665 union and intersection set of CNAs were further filtered to remove any segments under 10 Kbp.

666 Four pipeline combinations using PhyloWGS (v3b75ba9) and the intersection and union of SNVs  
667 and CNAs were executed on 293 single-region samples. The script `create_phylowgs_inputs.py`  
668 was used to combine intersect and union of SNVs and CNAs as inputs for PhyloWGS, where no  
669 cellularity estimate was provided as there was no obvious way to derive that for the intersect and  
670 union of CNAs. The pipelines were run with otherwise identical procedure as single-region  
671 reconstructions with PhyloWGS (v3b75ba9).

## 672 **Clonality Classification**

673 We classified the phylogenetic clone trees outputted by PhyloWGS (v3b75ba9) and mutation  
674 clustering results outputted by PyClone (v0.13.0), DPCLust (v2.2.5) and SciClone (v1.0.7) as  
675 monoclonal or polyclonal based on the number of subclones they predicted. Solutions where only  
676 one subclone was predicted were termed *monoclonal*. In monoclonal reconstructions, the only  
677 subclone detected is then termed the clonal node. Solutions where more than one subclone was  
678 predicted were termed *polyclonal*. In polyclonal reconstructions, the subclone with the highest  
679 cellular prevalence was deemed clonal, and the rest of the subclones were subclonal. In situations  
680 where PhyloWGS (v3b75ba9) outputted phylogenies showed a normal root node with more than  
681 one direct child, the clone tree was termed *polytumour*, suggestive of multiple independent primary  
682 tumours. These were excluded from downstream analysis because the reconstruction of these  
683 phylogenies, especially from single sequencing samples, is challenging<sup>13</sup>.



684 CNA and SNV mutations were classified as clonal or subclonal based on their node assignment in  
685 the best PhyloWGS (v3b75ba9) consensus clone tree and PyClone (v0.13.0), DPCLust (v2.2.5) and  
686 SciClone (v1.0.7) mutation clusters. The mutations that define the clonal node were classified as  
687 clonal mutations, while all others were classified as subclonal mutations. The cancer cell fraction  
688 (CCF) of mutations was calculated by dividing the cellular prevalence of the node that the mutation  
689 belonged to by the predicted cellularity of the tumour sample.

### 690 **Analysis of Single Nucleotide Variants**

691 We compared the four pipelines using each subclonal reconstruction algorithm for their inference  
692 of clonal and subclonal SNVs. In each pairwise comparison, for each sample we noted the clonal  
693 SNV set identified by each algorithm and calculated the Jaccard index between the two sets. The  
694 analysis was performed separately for clonal and subclonal SNVs.

### 695 **Analysis of Copy Number Aberrations**

696 We further filtered the CNAs identified by PhyloWGS using OncoScan data for samples with the  
697 data available, removing the identified CNAs that did not overlap any OncoScan CNAs<sup>13</sup>. For  
698 samples without OncoScan data, CNAs outputted by PhyloWGS (v3b75ba9) were filtered to retain  
699 only those across genomic locations with recurrence of CNAs in OncoScan-filtered samples, with  
700 10 being the established empirical recurrence threshold<sup>13</sup>. Bins of 1.0 Mbp were created across the  
701 genome to characterize the copy number profiles for each sample and were assigned the copy  
702 number of overlapping genomic segments, either neutral or mutated. Regions not considered by  
703 PhyloWGS (v3b75ba9) due to lack of information were assumed to have the normal copy number  
704 of two. Profiles were created separately for clonal and subclonal CNAs. We further used  
705 previously identified clonal and subclonal subtypes to cluster samples<sup>13</sup>. Samples that were  
706 assigned a subclonal subtype in the SomaticSniper-TITAN pipeline<sup>13</sup> but had no subclonal  
707 populations detected in another pipeline were excluded from subclonal subtype analysis for that  
708 pipeline. Samples that had no subclonal populations detected in the SomaticSniper-TITAN  
709 pipeline and were therefore never assigned to a subclonal subtype were not considered in any  
710 subclonal subtype analysis. For each pipeline, we used the copy number profiles of all samples  
711 with available data to generate average subtype-specific clonal and subclonal CNA profiles of  
712 localized prostate cancer, with standard deviation.

713 We compared the CNA profiles identified by the four PhyloWGS-comprising pipelines by  
714 assessing the difference in clonal and subclonal CNAs between pipeline pairs. For each sample, a  
715 clonal CNA set was generated from pipeline results, where the direction of the CNA is taken into  
716 account. For example, if a sample was identified with a clonal gain in genomic bin 1 and a clonal  
717 loss in genomic bin 2, it would have the clonal CNA set +1, -2. The Jaccard index of clonal and  
718 subclonal CNA sets for each sample were calculated between all pipeline pairs.

719 We identified CNAs that were differentially altered clonally and subclonally. Using 1.0 Mbp bins  
720 across the genome, we aggregated the number of samples with and without a CNA overlapping  
721 each 1.0 Mbp stretch, with gains and losses considered separately. Clonal and subclonal CNAs  
722 were annotated separately, and only samples with *polyclonal* phylogenies were considered, since  
723 they have both clonal and subclonal components. Pearson's  $\chi^2$  test was used with multiple testing  
724 correction (FDR  $\leq$  0.05) to define the bins that were significantly enriched for clonal or subclonal  
725 CNAs that were gain or loss. CNAs in these bins were thus considered significantly differentially  
726 altered, with a predisposition to occur clonally or subclonally as a gain or a loss. Genes affected  
727 by differentially altered CNAs were annotated using RefSeq, and the lists of genes considered to  
728 have CNA biases by the four pipelines were compared for overlap.

729 We performed pathway enrichment analysis on the genes that were identified by all four  
730 PhyloWGS-comprising pipelines as biased to be affected by CNAs clonally or subclonally. Using  
731 all default parameters of *gprofiler2* (v0.1.9) in R (v3.5.3)<sup>54</sup>, statistically significant pathways were  
732 obtained from the data sources Gene Ontology (Biological Process, Molecular Function and  
733 Cellular Component), KEGG and Reactome, with no electronic GO annotations. We discarded  
734 pathways that involved  $>350$  or  $< 5$  genes. Cytoscape (v3.4.0) was used to visualize significant  
735 pathways<sup>55</sup>. Since all genes identified as significantly differentially altered were biased to be  
736 altered clonally, we defined these pathways as differentially altered clonally.

### 737 **Driver Mutation Analysis**

738 We gathered a list of known prostate cancer driver genes based on previous large sequencing  
739 studies<sup>13,23</sup>. The known CNA-affected driver genes considered were *MYC*, *TP53*, *NKX3-1*, *RBI*,  
740 *CDKN1B*, *CHD1*, *PTEN* and *CDH1*. The known SNV-affected driver genes considered were *ATM*,  
741 *MED12*, *FOXA1*, *SPOP* and *TP53*. PhyloWGS-comprising pipelines identified CNAs overlapping  
742 CNA-affected driver genes and SNVs that occurred in SNV-affected driver genes. These were

743 defined to be driver CNAs and driver SNVs, respectively. A sample was considered to have a  
744 consensus driver mutation, CNA or SNV, if the mutation was identified with the same clonality  
745 by all four PhyloWGS-comprising pipelines.

746 Driver SNVs and CNAs of each sample were categorized by the number of PhyloWGS-comprising  
747 pipelines they were identified in. Since four PhyloWGS-comprising pipelines were used, in each  
748 sample driver SNVs and CNAs could be identified in all four pipelines, three pipelines, two  
749 pipelines or one pipeline. Proportions of each category were calculated by dividing the number of  
750 samples in that category by the sum of samples assigned to all categories for the driver SNV or  
751 CNA. The analysis was done separately for clonal and subclonal mutations, such that the category  
752 of the driver SNVs or CNAs in a sample was defined by the most frequent identification of the  
753 clonality. For example, if a driver SNV in a sample was identified as clonal by two pipelines,  
754 subclonal by one pipeline and wildtype by the last pipeline, it would be counted in both category  
755 two for the clonal analysis and in category one for the subclonal analysis.

## 756 **Biomarker Survival Analysis**

757 We assessed the utility of clonality (monoclonal vs. polyclonal) as a biomarker in all sixteen  
758 pipelines used for single region subclonal reconstruction of 293 samples. Tumours were grouped  
759 by clonality and the two groups were compared using a log-rank test for differences in outcome.  
760 Tumours were also grouped by integrating the previously defined multi-modal biomarker<sup>23</sup>  
761 (groups patients into low risk and high-risk) and clonality, creating unified groups (unified-low:  
762 monoclonal low-risk, unified-intermediate: monoclonal high-risk or polyclonal low-risk, unified-  
763 high: polyclonal high-risk)<sup>13</sup> that were compared using a log-rank test. Primary outcome as time  
764 to biochemical recurrence (BCR) was described in detail previously<sup>13</sup>. In brief, BCR was defined  
765 as PSA rise of  $\geq 2.0$  ng/mL above the nadir for radiotherapy patients and two-consecutive post-  
766 surgery PSA measurements  $> 0.2$  ng/mL (backdated to the date of first increase in PSA) for surgery  
767 patients. If a surgery patient had a post-operative PSA  $\geq 0.2$  ng/mL this was considered primary  
768 treatment failure. After salvage radiation therapy, if PSA continued to rise, BCR was backdated to  
769 the first PSA measurement  $> 0.2$  ng/mL, but if not then this was not considered a BCR.  
770 Salvage therapy (hormone therapy or chemotherapy) was considered a BCR.

## 771 **Comparing Reconstruction using Single and Multiple Regions**

772 For each of the 10 **tumours** with multi-region sequencing, we compared the subclonal  
773 reconstruction solutions from each single region with the solutions obtained from subclonal  
774 reconstruction using all tumour regions. In addition to number of subclones **predicted**, we  
775 compared SNV and CNA clonality **predictions** between single- and multi-region reconstructions.  
776 For all SNVs that were **identified** in a single-region **or** its corresponding multi-region  
777 reconstruction, we calculated the proportion of SNVs in each of the following categories:

- 778 1. Multi- and single-region **match: same SNV** clonality in single- and multi-region.
- 779 2. Clonal in multi-region: SNV **identified** in both single- and multi-region  
780 reconstructions, but **SNV** clonal in multi-region and subclonal in single-region.
- 781 3. Subclonal in multi-region: SNV **identified** in both single- and multi-region  
782 reconstructions, but **SNV** subclonal in multi-region and clonal in single-region.
- 783 4. Unique in single-region: SNV only present in single-region reconstruction.
- 784 5. Unique in multi-region: SNV only present in multi-region reconstruction.

785 Similarly, all CNAs that were **identified** in a single-region reconstruction **or** its matching multi-  
786 region reconstruction were assigned to categories defined in a similar fashion. Additional  
787 separation was added for CNAs **to distinguish between clonal and subclonal predictions**.

## 788 **Data Visualization and Reporting**

789 Data was visualized using the R statistical environment (v3.2.5 **or** v3.5.3), and performed using  
790 the lattice (v0.20-34), latticeExtra (v0.6-28), VennDiagram (v1.6.21)<sup>56</sup> and BPG (v5.3.4)<sup>57</sup>  
791 packages. All boxplots show the median (center line), upper and lower quartiles (box limits), and  
792 whiskers extend to the minimum and maximum values within 1.5 times the interquartile range  
793 (Tukey boxplots). Figures were compiled **in** Inkscape (v0.91). Standard deviation of the **sample**  
794 mean was reported for point estimates. All statistical tests were two-sided. **Supplementary File 1**  
795 **visualizes** all phylogenies **produced by pipelines using PhyloWGS**.

## 796 **List of abbreviations**

797 **CCF** - Cancer Cell Fraction  
798 **CNAs** - Copy Number Aberrations  
799 **II** - Intersect of SNVs and Intersect of CNAs  
800 **IU** - Intersect of SNVs and Union of CNAs  
801 **MB** - MuTect-Battenberg  
802 **MCMC** - Markov chain Monte Carlo  
803 **MF** - MuTect-FACETS  
804 **MT** - MuTect-TITAN

805 SB - SomaticSniper-Battenberg  
806 SD - standard deviation  
807 SF - SomaticSniper-FACETS  
808 SNVs - Single Nucleotide Variants  
809 ST - SomaticSniper-TITAN  
810 UI - Union of SNVs and Intersect of CNAs  
811 UU - Union of SNVs and Union of CNAs  
812 VAF - Variant Allele Frequency  
813 WGS -Whole-genome Sequencing  
814

## 815 **Data Availability**

816 Data supporting the conclusions of this article is included within it and its additional files, and at:  
817 EGAS00001000900

818 WGS Data - Baca *et al.*, 2013: dbGaP, phs000447.v1.p135

819 WGS Data – Berger *et al.*, 2011: dbGaP, phs000330.v1.p136

820 WGS Data – CPC-GENE Fraser *et al.*, 2017: EGA, EGAS00001000900; GEO: GSE8404323

821 WGS Data – The Cancer Genome Atlas Research Network, 2015:

822 <https://portal.gdc.cancer.gov/projects/TCGA-PRAD37>

823 WGS Data - Weischenfeldt *et al.*, 2013: EGA, EGAS0000100040038

824 WGS Data – CPC-GENE Espiritu *et al.*, 2018: EGA, EGAS0000100090013

825 WGS Data – CPC-GENE Taylor *et al.*, 2017: EGA, EGAS00001001615; EGA,

826 EGAS00001000025824

827 Variant Data - CPC-GENE Espiritu *et al.*, 2018: EGA, EGAS0000100090013

828 Source Data for Figures 4 and Supplementary Figures 4A, B, 5 are provided in Variant Data:

829 EGAS00001000900.

830 Source data for Figures 2, 3, 6A,C, 7A and Supplementary Figures 1, 2, 3A, 4C-F, 7A-C, 8B, 9,

831 10, 11, 12 are provided in Supplementary Tables 1-5.

832 Source data for Figures 5, 6B, 7B and Supplementary Figures 3B-E, 6, 8A, C, 13 are provided in

833 Source Data.

## 834 **Code availability**

835 Custom analysis & data-visualization code is available upon request.

836

## 837 **References**

- 838 1. Abbosh, C. *et al.* Phylogenetic ctDNA analysis depicts early-stage lung cancer evolution.  
839 *Nature* **545**, 446–451 (2017).
- 840 2. Jamal-Hanjani, M. *et al.* Tracking the Evolution of Non–Small-Cell Lung Cancer. *N. Engl.*  
841 *J. Med.* **376**, 2109–2121 (2017).
- 842 3. Turajlic, S. *et al.* Tracking Cancer Evolution Reveals Constrained Routes to Metastases:  
843 TRACERx Renal. *Cell* **173**, 581-594.e12 (2018).
- 844 4. Turajlic, S. *et al.* Deterministic Evolutionary Trajectories Influence Primary Tumor  
845 Growth: TRACERx Renal. *Cell* **173**, 595-610.e11 (2018).
- 846 5. Gudem, G. *et al.* The evolutionary history of lethal metastatic prostate cancer. *Nature* **520**,  
847 353–357 (2015).
- 848 6. Gerlinger, M. *et al.* Intratumor Heterogeneity and Branched Evolution Revealed by  
849 Multiregion Sequencing. *N. Engl. J. Med.* **366**, 883–892 (2012).
- 850 7. Nik-Zainal, S. *et al.* The life history of 21 breast cancers. *Cell* **149**, 994–1007 (2012).
- 851 8. Boutros, P. C. *et al.* Spatial genomic heterogeneity within localized, multifocal prostate  
852 cancer. *Nat. Genet.* **47**, 736–745 (2015).
- 853 9. Cooper, C. S. *et al.* Analysis of the genetic phylogeny of multifocal prostate cancer  
854 identifies multiple independent clonal expansions in neoplastic and morphologically normal  
855 prostate tissue. *Nat. Genet.* **47**, 367–372 (2015).
- 856 10. Mitchell, T. J. *et al.* Timing the Landmark Events in the Evolution of Clear Cell Renal Cell  
857 Cancer: TRACERx Renal. *Cell* **173**, 611-623.e17 (2018).
- 858 11. Gerlinger, M. *et al.* Genomic architecture and evolution of clear cell renal cell carcinomas  
859 defined by multiregion sequencing. *Nat. Genet.* **46**, 225–233 (2014).
- 860 12. Alves, J. M., Prieto, T. & Posada, D. Multiregional Tumor Trees Are Not Phylogenies.  
861 *Trends in Cancer* **3**, 546–550 (2017).
- 862 13. Espiritu, S. M. G. *et al.* The Evolutionary Landscape of Localized Prostate Cancers Drives  
863 Clinical Aggression. *Cell* **173**, 1003-1013.e15 (2018).

- 864 14. Jiao, W., Vembu, S., Deshwar, A. G., Stein, L. & Morris, Q. Inferring clonal evolution of  
865 tumors from single nucleotide somatic mutations. *BMC Bioinformatics* **15**, 35 (2014).
- 866 15. Deshwar, A. G. *et al.* PhyloWGS: Reconstructing subclonal composition and evolution  
867 from whole-genome sequencing of tumors. *Genome Biol.* **16**, 35 (2015).
- 868 16. Bolli, N. *et al.* Heterogeneity of genomic evolution and mutational profiles in multiple  
869 myeloma. *Nat. Commun.* **5**, (2014).
- 870 17. Roth, A. *et al.* PyClone: Statistical inference of clonal population structure in cancer. *Nat.*  
871 *Methods* **11**, 396–398 (2014).
- 872 18. Zare, H. *et al.* Inferring Clonal Composition from Multiple Sections of a Breast Cancer.  
873 *PLoS Comput. Biol.* **10**, e1003703 (2014).
- 874 19. Oesper, L., Mahmoody, A. & Raphael, B. J. THetA: Inferring intra-tumor heterogeneity  
875 from high-throughput DNA sequencing data. *Genome Biol.* **14**, R80 (2013).
- 876 20. Miller, C. A. *et al.* SciClone: Inferring Clonal Architecture and Tracking the Spatial and  
877 Temporal Patterns of Tumor Evolution. *PLoS Comput. Biol.* **10**, 1003665 (2014).
- 878 21. Jiang, Y., Qiu, Y., Minn, A. J. & Zhang, N. R. Assessing intratumor heterogeneity and  
879 tracking longitudinal and spatial clonal evolutionary history by next-generation sequencing.  
880 *Proc. Natl. Acad. Sci.* **113**, E5528–E5537 (2016).
- 881 22. Dentre, S. C. *et al.* Portraits of genetic intra-tumour heterogeneity and subclonal selection  
882 across cancer types. Preprint at *bioRxiv* doi:10.1101/312041 (2018).
- 883 23. Fraser, M. *et al.* Genomic hallmarks of localized, non-indolent prostate cancer. *Nature* **541**,  
884 359–364 (2017).
- 885 24. Taylor, R. A. *et al.* Germline BRCA2 mutations drive prostate cancers with distinct  
886 evolutionary trajectories. *Nat. Commun.* **8**, 13671 (2017).
- 887 25. Ha, G. *et al.* TITAN: Inference of copy number architectures in clonal cell populations from  
888 tumor whole-genome sequence data. *Genome Res.* **24**, 1881–1893 (2014).
- 889 26. Larson, D. E. *et al.* Somaticsniper: Identification of somatic point mutations in whole  
890 genome sequencing data. *Bioinformatics* **28**, 311–317 (2012).



- 891 27. Cibulskis, K. *et al.* Sensitive detection of somatic point mutations in impure and  
892 heterogeneous cancer samples. *Nat. Biotechnol.* **31**, 213–219 (2013).
- 893 28. Shen, R. & Seshan, V. E. FACETS: allele-specific copy number and clonal heterogeneity  
894 analysis tool for high-throughput DNA sequencing. *Nucleic Acids Res.* **44**, e131–e131  
895 (2016).
- 896 29. Qi, Y., Pradhan, D. & El-Kebir, M. Implications of non-uniqueness in phylogenetic  
897 deconvolution of bulk DNA samples of tumors. *Algorithms Mol. Biol.* **14**, 19 (2019).
- 898 30. Gerstung, M. *et al.* The evolutionary history of 2,658 cancers. *Nature* **578**, 122–128 (2020).
- 899 31. Ewing, A. D. *et al.* Combining tumor genome simulation with crowdsourcing to benchmark  
900 somatic single-nucleotide-variant detection. *Nat. Methods* **12**, 623–630 (2015).
- 901 32. Dentro, S. C., Wedge, D. C. & Van Loo, P. Principles of Reconstructing the Subclonal  
902 Architecture of Cancers. *Cold Spring Harb. Perspect. Med.* **7**, a026625 (2017).
- 903 33. Sun, R. *et al.* Between-region genetic divergence reflects the mode and tempo of tumor  
904 evolution. *Nat. Genet.* **49**, 1015–1024 (2017).
- 905 34. Salcedo, A. *et al.* A community effort to create standards for evaluating tumor subclonal  
906 reconstruction. *Nat. Biotechnol.* **38**, 97–107 (2020).
- 907 35. Baca, S. C. *et al.* Punctuated evolution of prostate cancer genomes. *Cell* **153**, 666–677  
908 (2013).
- 909 36. Berger, M. F. *et al.* The genomic complexity of primary human prostate cancer. *Nature* **470**,  
910 214–220 (2011).
- 911 37. The Cancer Genome Atlas Research Network. The Molecular Taxonomy of Primary  
912 Prostate Cancer. *Cell* **163**, 1011–1025 (2015).
- 913 38. Weischenfeldt, J. *et al.* Integrative Genomic Analyses Reveal an Androgen-Driven Somatic  
914 Alteration Landscape in Early-Onset Prostate Cancer. *Cancer Cell* **23**, 159–170 (2013).
- 915 39. Li, H. & Durbin, R. Fast and accurate short read alignment with Burrows-Wheeler  
916 transform. *Bioinformatics* **25**, 1754–1760 (2009).
- 917 40. McKenna, A. *et al.* The Genome Analysis Toolkit: a MapReduce framework for analyzing

- 918 next-generation DNA sequencing data. *Genome Res.* **20**, 1297–303 (2010).
- 919 41. Li, H. *et al.* The Sequence Alignment/Map format and SAMtools. *Bioinformatics* **25**, 2078–  
920 2079 (2009).
- 921 42. Cibulskis, K. *et al.* ContEst: Estimating cross-contamination of human samples in next-  
922 generation sequencing data. *Bioinformatics* **27**, 2601–2602 (2011).
- 923 43. Van Loo, P. *et al.* Allele-specific copy number analysis of tumors. *Proc. Natl. Acad. Sci.*  
924 **107**, 16910–16915 (2010).
- 925 44. Jafar Taghiyar, M. *et al.* Kronos: A workflow assembler for genome analytics and  
926 informatics. *Gigascience* **6**, 1–10 (2017).
- 927 45. Lai, D., Ha, G. & Shah, S. *HMMcopy: Copy number prediction with correction for GC and*  
928 *mappability bias for HTS data.* (2016).
- 929 46. Langmead, B., Trapnell, C., Pop, M. & Salzberg, S. L. Ultrafast and memory-efficient  
930 alignment of short DNA sequences to the human genome. *Genome Biol.* **10**, R25 (2009).
- 931 47. Ding, J. *et al.* Feature-based classifiers for somatic mutation detection in tumour-normal  
932 paired sequencing data. *Bioinformatics* **28**, 167–175 (2012).
- 933 48. Sherry, S. T. dbSNP: the NCBI database of genetic variation. *Nucleic Acids Res.* **29**, 308–  
934 311 (2001).
- 935 49. Forbes, S. A. *et al.* COSMIC: Exploring the world’s knowledge of somatic mutations in  
936 human cancer. *Nucleic Acids Res.* **43**, D805–D811 (2015).
- 937 50. Wang, K., Li, M. & Hakonarson, H. ANNOVAR: Functional annotation of genetic variants  
938 from high-throughput sequencing data. *Nucleic Acids Res.* **38**, e164–e164 (2010).
- 939 51. Lawrence, M. *et al.* Software for Computing and Annotating Genomic Ranges. *PLoS*  
940 *Comput. Biol.* **9**, e1003118 (2013).
- 941 52. Quinlan, A. R. & Hall, I. M. BEDTools: A flexible suite of utilities for comparing genomic  
942 features. *Bioinformatics* **26**, 841–842 (2010).
- 943 53. Haider, S. *et al.* A bedr way of genomic interval processing. *Source Code Biol. Med.* **11**, 14  
944 (2016).

- 945 54. Reimand, J., Kull, M., Peterson, H., Hansen, J. & Vilo, J. G:Profiler-a web-based toolset  
946 for functional profiling of gene lists from large-scale experiments. *Nucleic Acids Res.* **35**,  
947 W193-200 (2007).
- 948 55. Shannon, P. *et al.* Cytoscape: A software Environment for integrated models of  
949 biomolecular interaction networks. *Genome Res.* **13**, 2498–2504 (2003).
- 950 56. Chen, H. & Boutros, P. C. VennDiagram: A package for the generation of highly-  
951 customizable Venn and Euler diagrams in R. *BMC Bioinformatics* **12**, 35 (2011).
- 952 57. P'ng, C. *et al.* BPG: Seamless, automated and interactive visualization of scientific data.  
953 *BMC Bioinformatics* **20**, 42 (2019).
- 954
- 955

956 **End Notes**

957 **Ethics approval and consent to participate**

958 All tumour samples in this study were obtained with patient informed consent, with institutional  
959 Research Ethics Board approval (University Health Network, Centre Hospitalier Universitaire de  
960 Québec) and following ICGC guidelines.

961 **Conflict of interest**

962 All authors declare that they have no conflicts of interest.

963 **Funding**

964 This work was supported by Prostate Cancer Canada and is proudly funded by the Movember  
965 Foundation - Grant #RS2014-01 to PCB. PCB was supported by a Terry Fox Research Institute  
966 and CIHR New Investigator Awards. This work was supported by NSERC Discovery Grants to  
967 QDM and PCB. This research is funded by the Canadian Cancer Society (grant #705649) and a  
968 Project Grant from CIHR. This work was funded by the Government of Canada through Genome  
969 Canada (OGI-125). VB, LYL and AS were supported by Fellowships from the Canadian Institutes  
970 of Health Research. The results described here are in part based upon data generated by the TCGA  
971 Research Network: <http://cancergenome.nih.gov/>. This work was supported by the NIH/NCI under  
972 awards P30CA016042, 1U01CA214194-01, 1U24CA248265-01 and 1R01CA244729-01.

973 **Author contributions**

974 Initiated the Project: VB, LYL, QDM, PCB  
975 Data Analyses: LYL, VB, SMGE  
976 Data Visualization: LYL, VB, AS  
977 Supervised Research: QDM, TK, PCB  
978 Wrote the First Draft of the Manuscript: VB, LYL, PCB  
979 Approved the Manuscript: All Authors

980 **Acknowledgements**

981 The authors thank Dr. Reimand (University of Toronto) for technical support. We also thank all  
982 members of the Boutros and Kislinger labs for helpful suggestions and technical support.

983

## 984 **Figure Legends**

### 985 **Figure 1 – Reconstruction Workflow and Experimental Design**

986 Raw sequencing data from the tumour and normal samples were aligned against the hg19 build of  
987 the human genome using bwa-aln and GATK. Somatic SNVs were **detected** using SomaticSniper  
988 and MuTect and annotated for function. Somatic CNAs were **detected** using TITAN, Battenberg  
989 **and FACETS** and filtered. All single region tumour samples had their subclonal architectures  
990 reconstructed using **sixteen** pipelines **combining one of SomaticSniper and MuTect, one of**  
991 **Battenberg and TITAN, and one of PyClone, PhyloWGS, DPClust and SciClone.** For tumours  
992 with samples from multiple regions, reconstructions of subclonal architectures were performed by  
993 considering **each individual region separately and by considering samples from all regions together**  
994 **using eighteen pipelines.**

### 995 **Figure 2 – Cellularity Estimates**

996 Cellularity of samples as estimated by the CNA detection tool and by subclonal reconstruction  
997 pipelines using the CNA detection tool Battenberg **A)** and TITAN **B)**. Each dot represents the  
998 estimate for a sample and colors delineate subclonal reconstruction algorithms. Mutation detection  
999 tool combinations using Battenberg include SomaticSniper-Battenberg and MuTect-Battenberg,  
1000 and mutation detection tool combinations using TITAN include SomaticSniper-TITAN and  
1001 MuTect-TITAN. Samples are ordered by cellularity estimates by the CNA detection tool. The  
1002 horizontal line indicates CNA detection tool estimated cellularity 0.75.

### 1003 **Figure 3 – Number of Subclones Detected**

1004 Each panel compares the number of subclones predicted for each sample by subclonal  
1005 reconstruction pipelines using the same mutation detection tool combinations SomaticSniper-  
1006 Battenberg **A)**, SomaticSniper-TITAN **B)**, MuTect-Battenberg **C)** and MuTect-TITAN **D)**. Each  
1007 marker represents the prediction for a sample, and the color of the marker represents the subclonal  
1008 reconstruction algorithm. In cases where algorithms predicted the same number of subclones, the  
1009 markers were randomly overlaid. Background color indicates the maximum number of subclonal  
1010 reconstruction algorithms that predicted the same number of subclones for that sample.

1011 **Figure 4 – SomaticSniper and MuTect**

1012 **A)** Density plots of variant allele frequencies for SNVs across all samples that were detected by  
1013 both SomaticSniper and MuTect (Intersect), only detected by MuTect (MuTect Unique) and only  
1014 detected by SomaticSniper (SomaticSniper Unique). **B)** Trinucleotide profile of SNVs that were  
1015 detected by both SomaticSniper and MuTect, where the number of SNVs was normalized by the  
1016 expected number of each trinucleotide context across the hg19 genome. Trinucleotide profiles for  
1017 SNVs only detected by SomaticSniper **C)** and SNVs only detected by MuTect **D)**.

1018 **Figure 5 – Clonal and Subclonal SNVs**

1019 Total number of clonal and subclonal SNVs identified by pipelines using DPClust **A)**, PhyloWGS  
1020 **B)**, PyClone **C)** and SciClone **D)**. Each stacked bar represents one sample and samples are ordered  
1021 based on the total number of SNVs identified by the pipeline using SomaticSniper and TITAN.  
1022 Color of the stacked bar reflects the clonality of the SNVs it represents (clonal or subclonal). **E)**  
1023 Jaccard index of pipeline-identified clonal and subclonal SNVs. Each marker represents a pipeline  
1024 pair that is compared, and the x- and y- axis show subclonal and clonal mean SNV Jaccard indices  
1025 across samples, respectively, with error bars indicating one standard deviation. ST, SomaticSniper-  
1026 TITAN; MT, MuTect-TITAN; SB, SomaticSniper-Battenberg; MB, MuTect-Battenberg.

1027 **Figure 6 - Single- and Multi-Region Reconstructions by PhyloWGS**

1028 **A)** Comparison of the number of subclones predicted by pipelines using PhyloWGS for each  
1029 tumour from multi-region reconstruction and reconstructions of each of the individual regions,  
1030 including the index lesion. Missing values indicate a failed reconstruction. **B)** Clonality of SNVs  
1031 identified by single-region and multi-region reconstructions. Variants were compared at position  
1032 level. Each single-region reconstruction is compared to the multi-region reconstruction of the same  
1033 tumour. SNVs were grouped into five categories: ‘Match in Multi and Single’ if the SNV was  
1034 predicted to be the same clonality in single- and multi-region reconstructions, ‘Clonal in Multi-  
1035 region’ if the SNV was clonal in multi-region reconstruction but subclonal in single-region  
1036 reconstruction, and ‘Subclonal in Multi-region’ if *vice versa*. If a SNV was only analyzed in single-  
1037 region reconstruction, it is ‘Unique in Single-region’, while SNVs only analyzed in multi-region  
1038 reconstruction are ‘Unique in Multi-region’. **C)** The disagreement in clonal and subclonal CNA  
1039 clonality predictions between single- and multi-region subclonal reconstructions. CNAs are

1040 compared by 1.0 Mbp genomic bins between single-region reconstructions and their corresponding  
1041 multi-region reconstructions. Categories are similar to those for SNVs.

1042 **Figure 7 - Single- and Multi-Region Reconstructions by PyClone**

1043 **A)** Number of subclones predicted by pipelines using PyClone for each tumour from multi-region  
1044 reconstruction and reconstructions of each of the individual regions, including the index lesion.  
1045 Missing values indicate a failed reconstruction. **B)** Clonality of SNVs identified by single-region  
1046 and multi-region reconstructions. Variants were compared at position level and each single-region  
1047 reconstruction is compared to the multi-region reconstruction of the same tumour. Match in Multi  
1048 and Single: SNVs predicted to be the same clonality in single- and multi-region reconstructions;  
1049 Clonal in Multi-region: SNVs clonal in multi-region reconstruction but subclonal in single-region  
1050 reconstruction; Subclonal in Multi-region: SNVs subclonal in multi-region reconstruction but  
1051 clonal in single-region reconstruction; Unique in Single-region: SNVs only analyzed in single-  
1052 region reconstruction; Unique in Multi-region: SNVs only analyzed in multi-region  
1053 reconstruction.

1054

## 1055 **Source Data**

### 1056 **Source Data 1 – Sample Subclonal Architecture Reports**

1057 Subclonal reconstruction solutions from four pipelines using PhyloWGS for 293 samples with  
1058 single-region sequencing, followed by 10 samples with multi-region sequencing. The first page  
1059 contains a legend explaining the components of single- and multi-region subclonal reconstruction  
1060 figures. Subsequent pages have details for all single-region samples followed by details for single-  
1061 and multi-region reconstructions for all multi-region samples.

### 1062 **Source Data 2 – Sample SNV Data**

1063 SNV reconstruction solutions for 293 samples with single-region sequencing and 10 samples with  
1064 multi-region sequencing, combined across all subclonal reconstruction pipelines. A SNV is present  
1065 if it was used by any pipeline and represented by chromosome and position. For all pipelines that  
1066 predicted the clonality of each SNV, the SNV is annotated with the predicted cancer cell fraction  
1067 from the pipeline, where a cancer cell fraction of 1 indicates that the SNV is clonal.

### 1068 **Source Data 3 – Sample Tree Summary**

1069 Subclonal architecture solutions for 293 samples with single-region sequencing in pipelines using  
1070 PhyloWGS, presented in the format (.json) as outputted by PhyloWGS. A file is presented for  
1071 every PhyloWGS-comprising pipeline that each sample was successfully executed in. The json  
1072 file contains subclonal architecture predictions across the 2500 MCMC iterations of PhyloWGS  
1073 and their log likelihoods.



# Figure 1

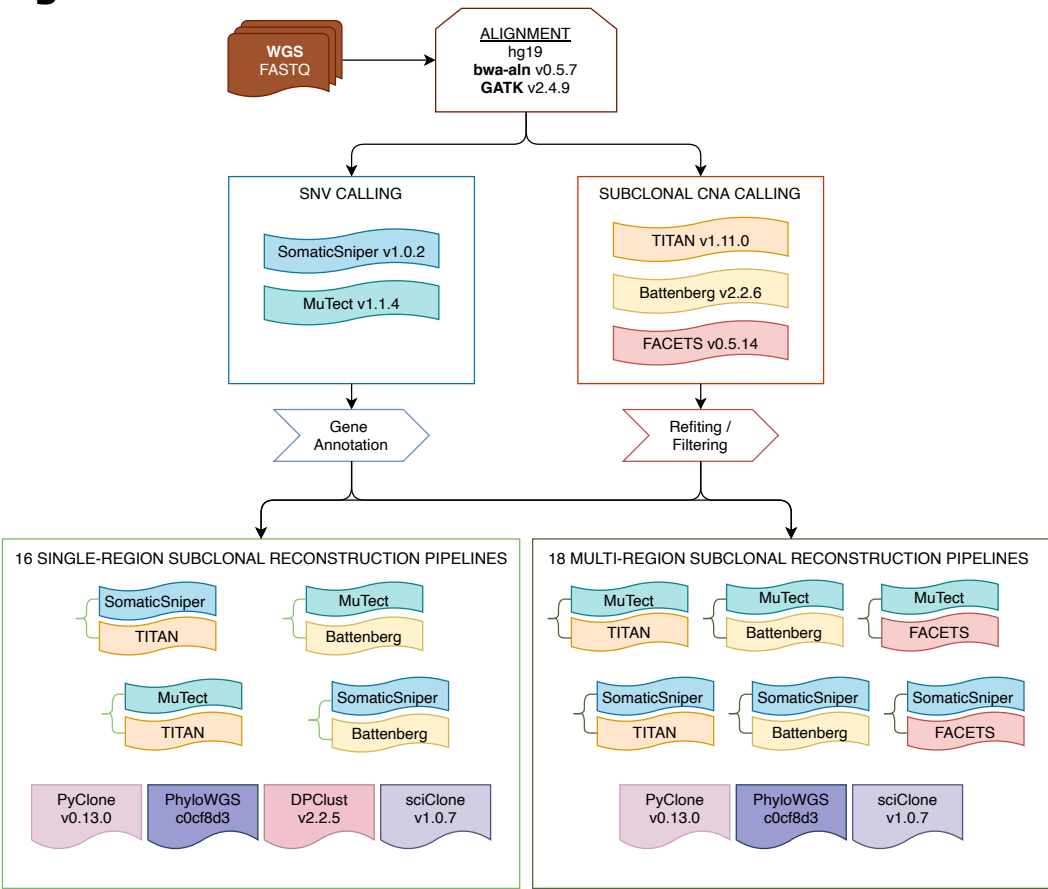
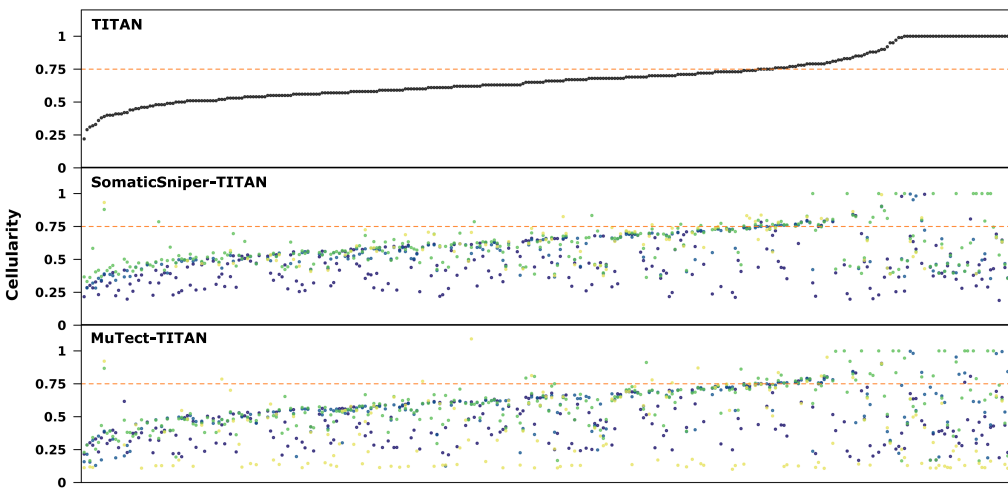
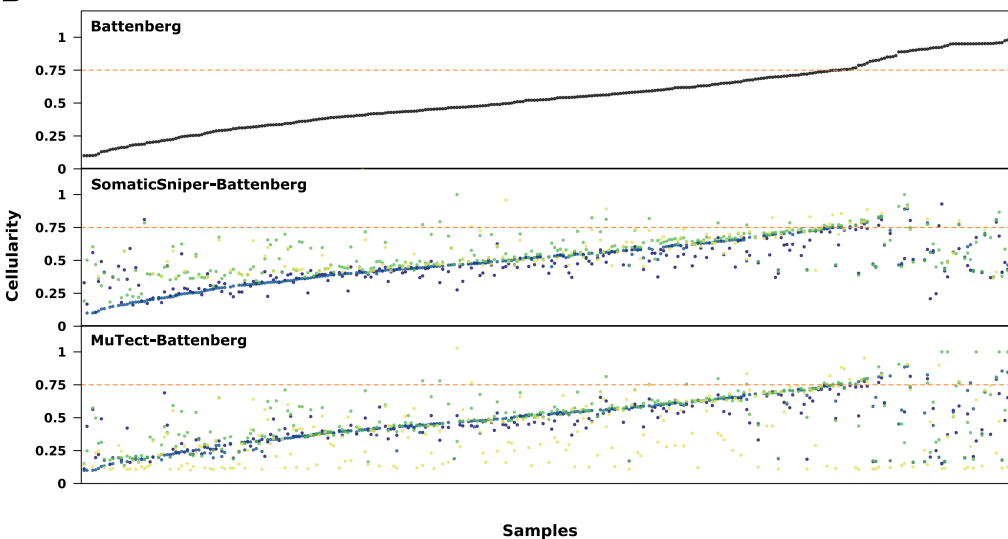


# Figure 2

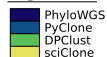
## A

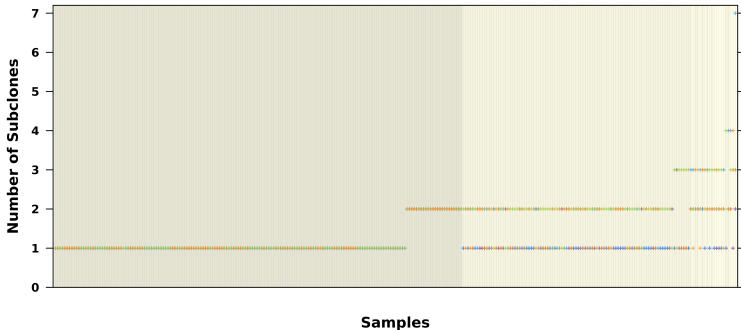
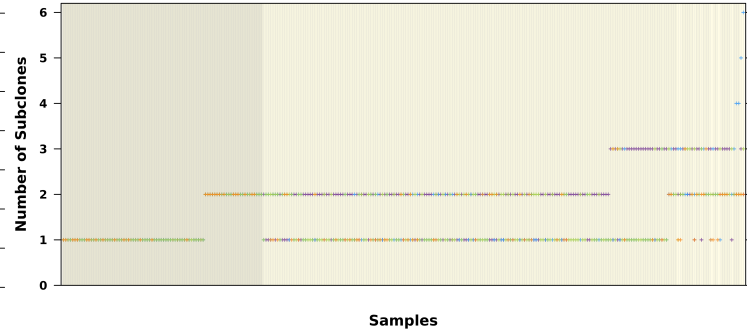
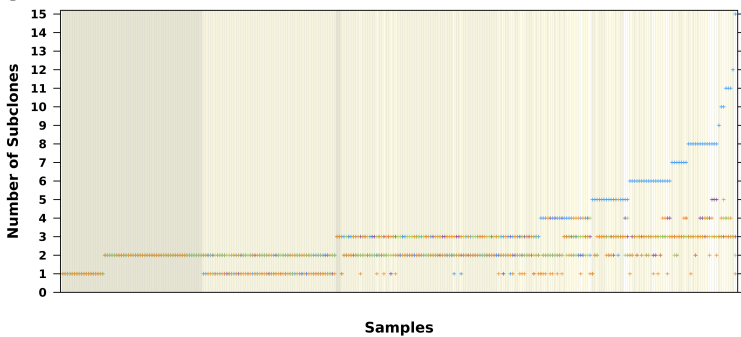
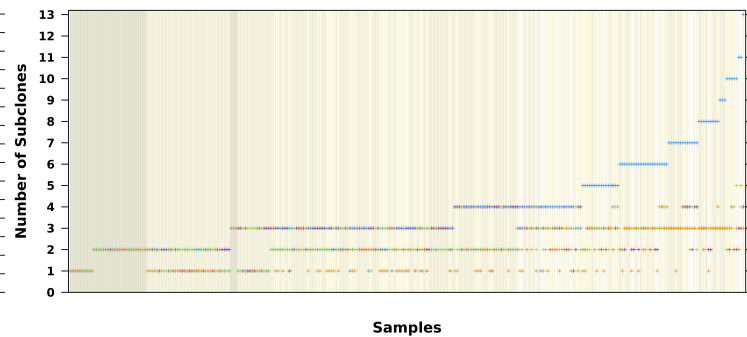
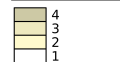


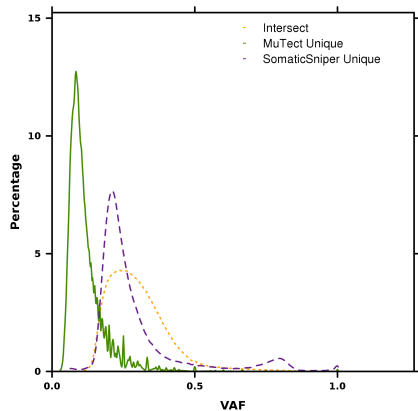
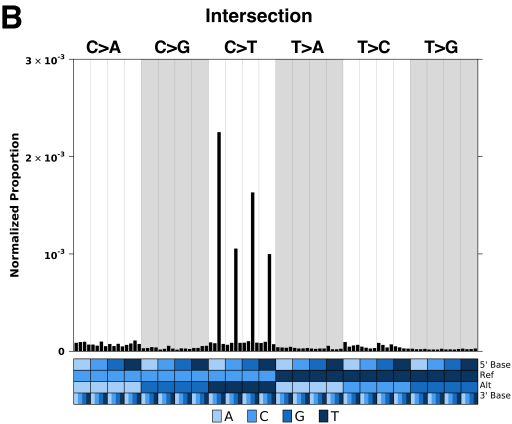
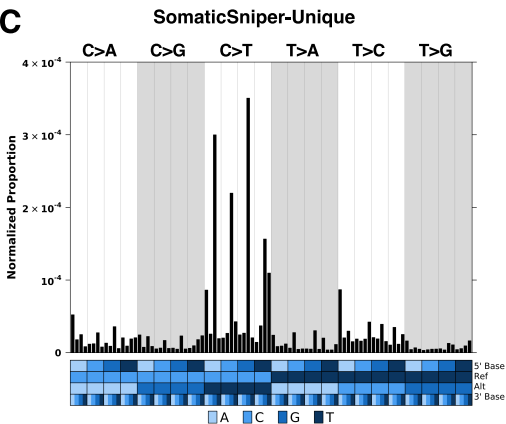
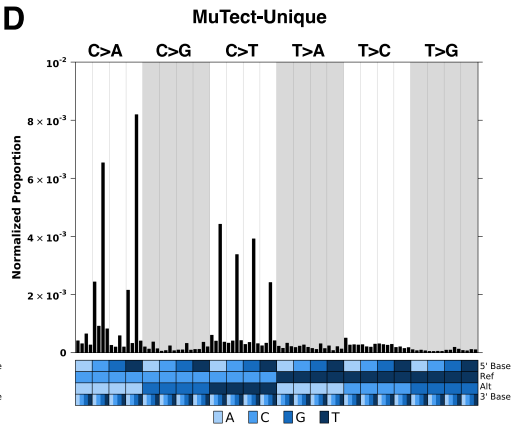
## B

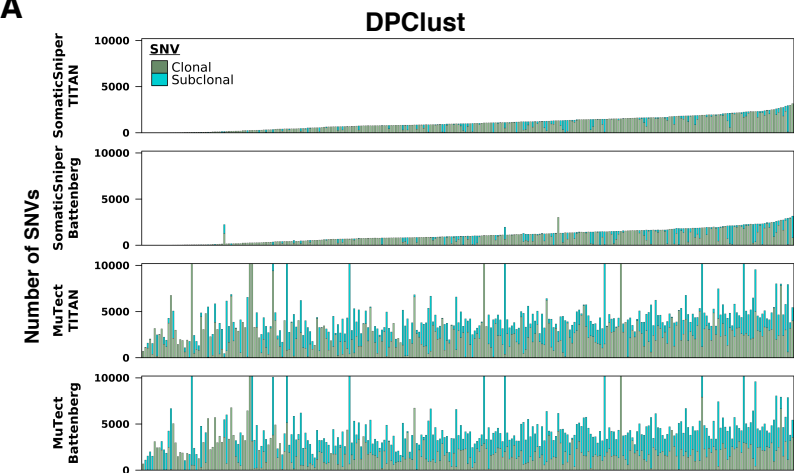
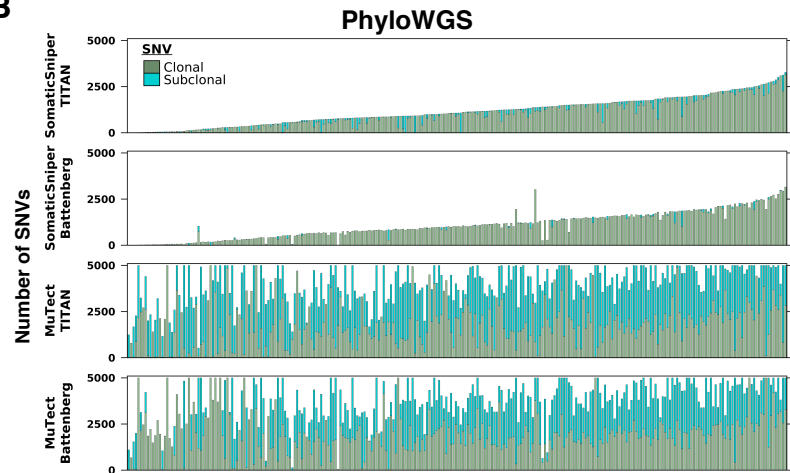
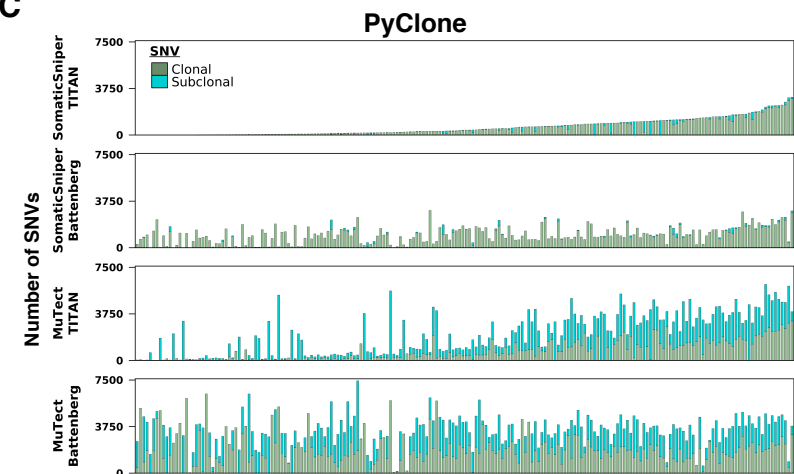
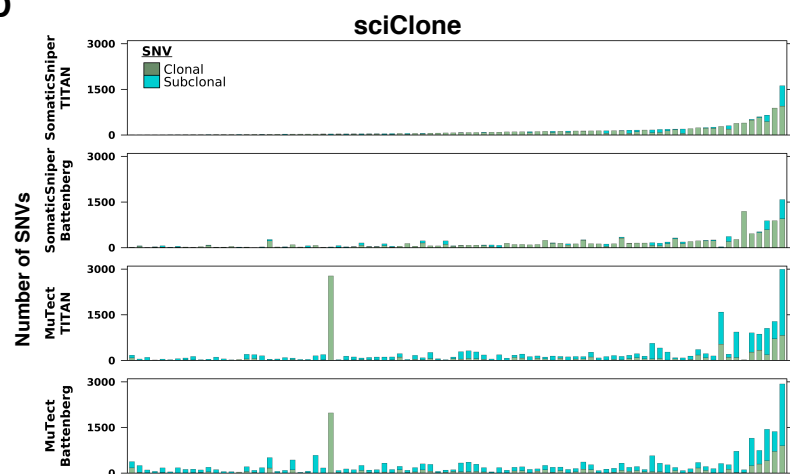
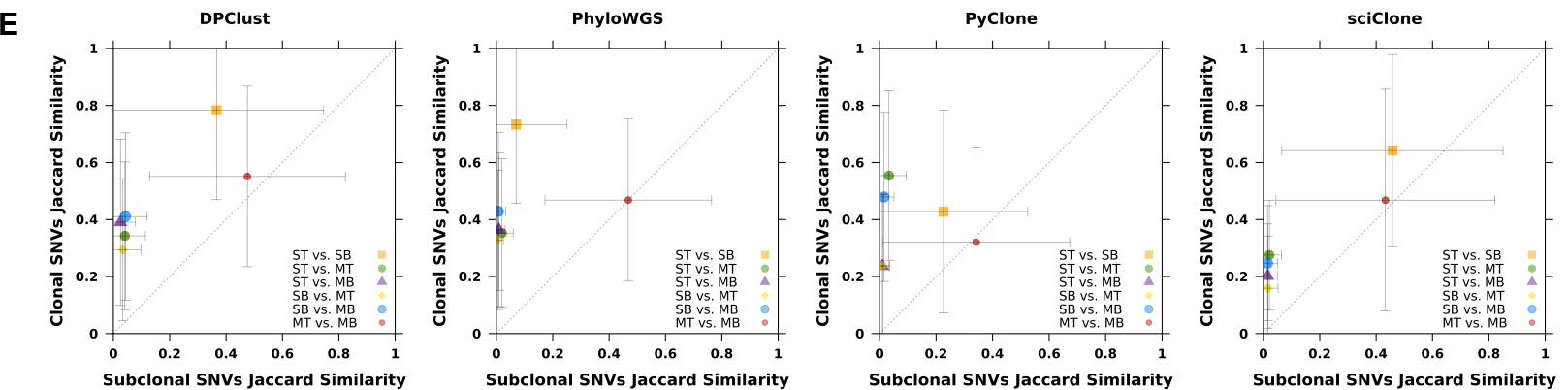


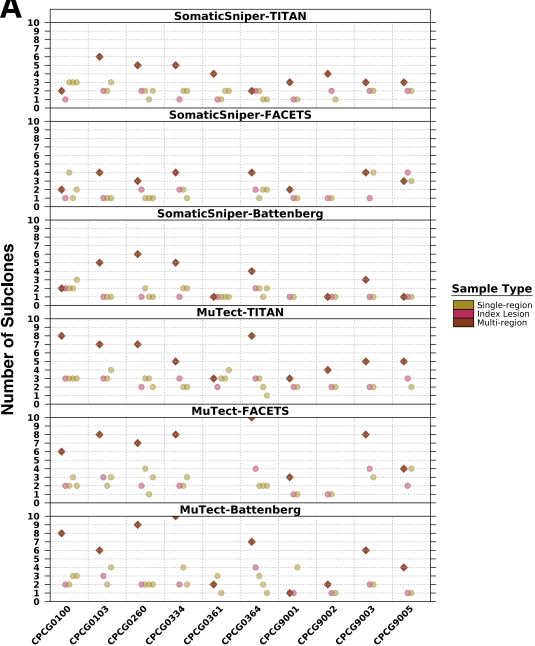
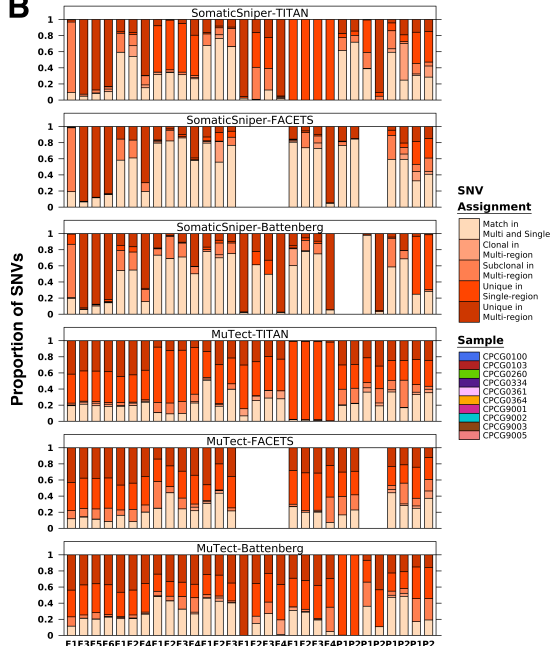
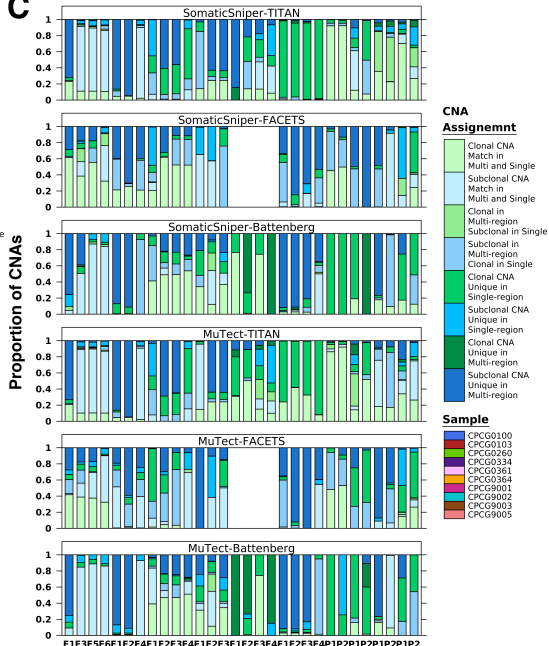
**Algorithm**



**Figure 3****A****SomaticSniper-Battenberg****B****SomaticSniper-TITAN****Algorithm****C****MuTect-Battenberg****D****MuTect-TITAN****Agreement**

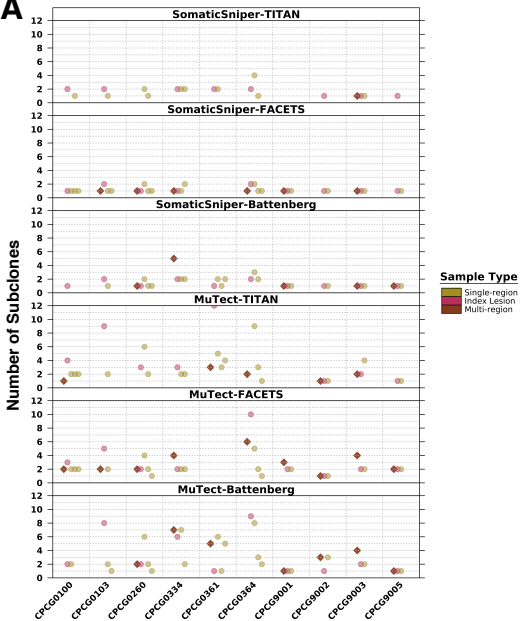
**Figure 4****A****B****C****D**

**Figure 5****A****B****C****D****E**

**Figure 6****A****B****C**

# Figure 7

## A



## B

